Aproximações quadráticas para análise de AVO de ondas convertidas

Darcicléa Ferreira Santos, darci@ufpa .br, *Pós-graduação/Geofísica/UFPa*
João dos Santos.Protázio, protazio@ufpa.br, *Matemática/UFPa*..
Jessé Carvalho Costa, jesse@ufpa .br, *Física/UFPa*.
Ellen de Nazaré Souza Gomes, ellensg@ufpa .br, *Matemática/UFPa*.

Abstract

Linearized approximations for reflections coefficients used for AVO analysis are not suitable to determine density contrasts. Second order approximations of converted waves reflected amplitudes are necessary to estimate density and the lithological indicators associated to it. We present explicit second order expression for reflected and transmitted amplitudes of converted waves in isotropic media which can be used to extend AVO analysis accurately to converted waves.

Introdução

A análise de AVO é baseada, em geral, em aproximações linearizadas das equações de Knott-Zoeppritz e são válidas apenas para pequenos contrastes dos parâmetros físicos através da interface e para incidências sub-normais (Castagna, 1993). Por outro lado, nem todos os contrastes físicos podem ser estimados com a inversão linearizada, especialmente o contraste de densidade (Lines, 1998), que revela importantes informações sobre a presença e saturação de hidrocarboneto. Logo, aproximações além de linearizações são desejáveis. Extensões quadráticas destas aproximações foram desenvolvidas recentemente para as amplitudes dos coeficientes de reflexão e de transmissão de uma onda incidente P (R_{pp} e T_{pp}), permitindo a obtenção de aproximações dessas amplitudes em termos de expressões quadráticas dos contrastes relativos dos meios (Wang, 1999). Por outro lado, as anomalias de AVO produzidas em eventos PP não distinguem o grau de saturação de gás em arenitos (Castagna et. al., 1998). Como as amplitudes das ondas convertidas R_{sp} são controladas, principalmente, pelos contrastes de densidade e de velocidade da onda S, a análise de AVO das ondas convertidas apresenta potencialidades não apenas para a discriminação de saturação de gás em arenitos mas também para predizer a porosidade e estimar o conteúdo de saturação de gás (Wu, 2000).
Neste trabalho são obtidas aproximações em termos de expressões quadráticas dos contrastes relativos para as amplitudes de ondas convertidas R_{sp} e T_{sp} em meios homogêneos e isotrópicos, considerando-se incidências sub-normais. Versões linearizadas destas aproximações são obtidas e resultados numéricos comparativos para os dois níveis de aproximações são apresentados.

Obtenção exata das amplitudes R_{sp} e T_{sp} a partir das equações de Zoeppritz para meios isotrópicos.

Consideremos o espalhamento de ondas planas através de uma interface plana horizontal que separa dois meios isotrópicos homogêneos, sendo ρ_1, α_1 e β_1, a densidade, a P-velocidade e a S-velocidade do meio incidente e ρ_2, α_2 e β_2, a densidade, a P-velocidade e a S-velocidade do meio subjacente, respectivamente. Definindo por s o parâmetro do raio, que corresponde à componente horizontal do vetor de vagarosidade, as amplitudes das ondas planas espalhadas são dadas de forma exata através das equações generalizadas de Zoeppritz (Schoenberg & Protázio, 1992):

$$\begin{aligned} \mathbf{X}_1(\mathbf{i}+\mathbf{r}) &= \mathbf{X}_2\mathbf{t} \\ \mathbf{Y}_1(\mathbf{i}-\mathbf{r}) &= \mathbf{Y}_2\mathbf{t}, \end{aligned} \tag{1}$$

sendo

$$\mathbf{X}_i = \begin{bmatrix} \alpha_i s & q_{3si} \\ -\rho_i\alpha_i(1-2\beta_i^2 s^2) & 2\rho_i\beta_i^2 s q_{3si} \end{bmatrix} \tag{2}$$

e

$$\mathbf{Y}_i = \begin{bmatrix} -2\rho_i\beta_i^2 s q_{3pi} & -\rho_i\beta_i(1-2\beta_i^2 s^2) \\ q_{3pi} & -\beta_i s \end{bmatrix} \tag{3}$$

as matrizes de impedância associadas aos meios incidente (i = 1) e subjacente (i = 2), $\mathbf{i}, \mathbf{r}$ e $\mathbf{t}$ as amplitudes das ondas incidente, refletida e transmitida, respectivamente. Nas expressões acima temos que

$$\begin{aligned} q_{3pi} &= (1-\alpha_i^2 s^2)^{1/2} \\ q_{3si} &= (1-\beta_i^2 s^2)^{1/2}. \end{aligned} \tag{4}$$

Considerando possíveis as inversões das matrizes envolvidas, as amplitudes das ondas refletidas e transmitidas são dadas pelas fórmulas

$$\begin{aligned} \mathbf{r} &= (\mathbf{X}_1^{-1}\mathbf{X}_2 - \mathbf{Y}_1^{-1}\mathbf{Y}_2)(\mathbf{X}_1^{-1}\mathbf{X}_2 + \mathbf{Y}_1^{-1}\mathbf{Y}_2)^{-1}\mathbf{i} \equiv \mathbf{R}\mathbf{i} \\ \mathbf{t} &= 2(\mathbf{X}_1^{-1}\mathbf{X}_2 + \mathbf{Y}_1^{-1}\mathbf{Y}_2)^{-1}\mathbf{i} \equiv \mathbf{T}\mathbf{i}. \end{aligned} \tag{5}$$

As estruturas das matrizes $\mathbf{R}$ e $\mathbf{T}$ são dadas por

$$\mathbf{R} = \begin{bmatrix} R_{pp} & R_{ps} \\ R_{sp} & R_{ss} \end{bmatrix} \quad \text{e} \quad \mathbf{T} = \begin{bmatrix} T_{pp} & T_{ps} \\ T_{sp} & T_{ss} \end{bmatrix} \tag{6}$$

em que o segundo subíndice corresponde ao tipo de onda incidente e o primeiro, ao tipo de onda espalha-

da. Neste trabalho, estamos interessados nas amplitudes R_{sp} e T_{sp}, que são calculadas a partir das expressões acima.

As fórmulas aproximadas para os coeficientes R_{sp} e T_{sp}.

Para uma onda incidente P, o parâmetro do raio (s) é dado por

$$s = \frac{\sin\theta}{\alpha_1}, \qquad (7)$$

em que θ é o ângulo de incidência e α_1 é a velocidade da onda P incidente. As aproximações dos coeficientes R_{sp} e T_{sp} respectivamente são dadas por:

$$\begin{aligned} R_{sp}(\theta) &\cong 2\sin\theta\left[\overline{R}_{sp0} + \frac{\overline{R}_{sp2}}{\alpha_1^2}\sin^2\theta\right] \\ T_{sp}(\theta) &\cong -2\rho_1\sin\theta\left[\overline{T}_{sp0} + \frac{\overline{T}_{sp2}}{\alpha_1^2}\sin^2\theta\right] \end{aligned} \qquad (8)$$

A partir da equação (8) são obtidas aproximações de primeira e segunda ordens dos coeficientes de reflexão e transmissão, obtidos em termos dos contrastes médios relativos dos parâmetros físicos envolvidos. Para isto, sendo x_1 e x_2 duas grandezas arbitrárias, definimos

$$\begin{aligned} \delta x &= \frac{x_2 - x_1}{2} \qquad \text{(contraste médio)} \\ \overline{x} &= \frac{x_2 + x_1}{2} \qquad \text{(valor médio).} \end{aligned} \qquad (9)$$

O contraste médio relativo é definido por :

$$\overline{\delta x} = \frac{\delta x}{\overline{x}}. \qquad (10)$$

No caso dos contrastes relativos entre os meios serem pequenos as fórmulas linearizadas são dadas por:

$$\overline{R}_{sp0} \cong -1/2\left[\overline{\delta\rho} + 2k(\overline{\delta\rho} + 2\,\overline{\delta\beta})\right] \qquad (11)$$

$$\overline{T}_{sp0} \cong \overline{\delta\rho} - 2\,k\,(\,\overline{\delta\rho} + 2\,\overline{\delta\beta}\,) \qquad (12)$$

$$\frac{\overline{R}_{sp2}}{\alpha_1^2} \cong k/4\left[\,2(1+2\,k)\,(\overline{\delta\rho} + 2\overline{\delta\beta}) - k\overline{\delta\rho}\,\right] \qquad (13)$$

e

$$\frac{\overline{T}_{sp2}}{\alpha_1^2} \cong \left(k^2/2\right)\overline{\delta\rho} - k(1-2k)(\overline{\delta\rho} + 2\overline{\delta\beta}). \qquad (14)$$

Para contrastes moderados as aproximações quadráticas são mais adequadas. Estas aproximações são dadas por:

$$\begin{aligned} R_{sp0} \cong -1/2\,\big[&\overline{\delta\rho}\,(1 + \overline{\delta\rho} + \overline{\delta\alpha} + \overline{\delta\beta}\,) \\ &+ 2k(1 - \overline{\delta\rho}\,)(\overline{\delta\rho} + 2\overline{\delta\beta}\,)\big] \end{aligned} \qquad (15)$$

$$\begin{aligned} T_{sp0} \cong\ &\overline{\delta\rho}\,(1 - \overline{\delta\rho} + \overline{\delta\alpha} - \overline{\delta\beta}\,) - \\ &2\,k\,(1 - \overline{\delta\rho}\,)\,(\,\overline{\delta\rho} + 2\,\overline{\delta\beta}\,) \end{aligned} \qquad (16)$$

$$\begin{aligned} \frac{\overline{R}_{sp2}}{\alpha_1^2} \cong\ &-(1/2)\,\overline{\delta\rho}\,\overline{\delta\alpha} + (k/2)(\,\overline{\delta\rho} + 2\,\overline{\delta\beta}\,) \\ &(1 - \overline{\delta\rho} + 2\,\overline{\delta\alpha}\,) + (k^2/4)\big[\,4\,(\overline{\delta\rho} + 2\,\overline{\delta\beta}\,) \\ &(1 + 3\,\overline{\delta\rho} + 3\,\overline{\delta\alpha} + \overline{\delta\beta}\,) - \overline{\delta\rho}\,(1 + \overline{\delta\rho} + 3\,\overline{\delta\alpha} + \overline{\delta\beta}\,)\,\big] \\ &+ k^3\,(\,\overline{\delta\rho} + 2\,\overline{\delta\beta}\,)\big[\,\overline{\delta\beta} - 4\,(\,\overline{\delta\rho} + 2\overline{\delta\beta}\,)\big] \end{aligned} \qquad (17)$$

$$\begin{aligned} \frac{\overline{T}_{sp2}}{\alpha_1^2} \cong\ &k\,(1-k)\,\big[(1-k)\,(1 - \overline{\delta\rho}\,) + 2\,(2-k)\,\overline{\delta\alpha} \\ &+ 2\,k\,\overline{\delta\beta}\,\big](\overline{\delta\rho} + 2\,\overline{\delta\beta}) + \big[\,k^2(1 - \overline{\delta\rho}\,) \\ &+ 2(1 + k^2)\,\overline{\delta\alpha}\big]\big[\,(1/2)\,\overline{\delta\rho} - k\,(\overline{\delta\rho} + 2\,\overline{\delta\beta})\big] \\ &+ \left(k^2/2\right)\overline{\delta\rho}\,(\overline{\delta\alpha} - \overline{\delta\beta}), \end{aligned} \qquad (18)$$

sendo $k = \frac{\overline{\beta}}{\overline{\alpha}}$ a importante relação entre as velocidades das ondas cisalhante e compressional.

Exemplos Numéricos.

A precisão das aproximações quadráticas e lineares é avaliada através de dois modelos sintéticos onde a variação dos ângulos de incidência é tomada no intervalo [0º, 30º].
No primeiro modelo, o meio incidente é um folhelho e no meio subjacente tem-se um arenito. No segundo modelo, o meio incidente é um anidrito e o meio subjacente é um calcário. Os parâmetros físicos dos dois modelos são apresentados na tabela 1 (Wang , 1999).

Tabela 1. Parâmetros para o cálculo dos coeficientes R_{sp} e T_{sp}.

Material	ρ (g/cm^3)	α (m/seg)	β (m/seg)
Arenito	2.65	3780	2360
Calcário	2.75	3845	2220
Folhelho	2.25	3600	1585
Anidrito	2.95	6095	3770

Os contrastes do primeiro modelo são baixos, enquanto que, no segundo, eles são moderados. A amplitude de R_{sp} mostrada na Figura 1 corresponde a um modelo de baixo contraste. Verifica-se que a fórmula quadrática para incidências de até 20º apresenta erros percentuais de no máximo 1%, enquanto que a aproximação linear apresenta erros da ordem de 1.6%. Para as amplitudes T_{sp} (Figura 2) para as mesmas incidências o erro percentual máximo é de 1% para a aproximação quadrática e 5% para a aproximação linear. Para o modelo 2, onde os contrates são moderados, verifica-se que as duas aproximação apresentam erros percentuais relativos iguais e abaixo de 1% (Figura 3 e Figura 4). Os resultados obtidos mostram que as duas aproximações apresentam boa precisão, desde que os pressupostos sejam observados.

Conclusão

Em análise de AVO são utilizadas, em geral, aproximações linearizadas das equações de Knott-Zoeppritz, mas que são bastante restritas por só terem validade em modelos com baixos contrastes dos parâmetros físicos e ângulos de incidência sub-normais. Por outro lado, a inversão de eventos PP não permite a estimativa dos contrastes de certos parâmetros relevantes, a densidade, por exemplo. O uso de aproximações além de linearizações e de AVO de ondas convertidas ganham grande importância. Neste trabalho, fórmulas aproximadas para AVO em termos de expressões quadráticas dos contrastes físicos e suas versões linearizadas são apresentadas. Os resultados mostram-se muitos bons considerando-se modelos com contrastes fracos e moderados.

Referências

Castagna, J.P., 1993, AVO Analysis - Tutorial and Review. In Castagna, J.P. & Backus, M..M. Eds. Offset-dependent reflectivity-Theory and pratice AVO analysis: SEG: P. 3 - 35.

Castagna, J.P., Swan, H.W. and Foster, D., 1998, Framework for AVO gradient intercept interpretation. Geophysics, 63, 948-956.

Lavaud, B., Kabir, N., and Chavent, G., 1999, Pushing AVO inversion beyond linearized approximation, Journal of Seismic Exploration, vol. 8, pp. 279 - 302

Lines, L. G., 1998, Density contrast is difficult to determine from AVO, CREWES Research Report, 10, pp. 47-1 47-8.

Schoenberg, M. and Protázio, J.S., 1992, Zoeppritz Rationalized and Generalized to Anisotropy: Journal of Seismic, no. 1, 125 - 144.

Wang, Y., 1999, Approximations to the Zoeppritz equations and their use in AVO analysis: Geophysics, Vol. 64, no. 6, P. 1920 - 1927.

Wu, Y., 2000, Estimation of gas saturation using P-to-S converted waves, Annual Meeting SEG / Calgary 2000.

Agradecimentos

Os autores agradecem ao suporte financeiro do Projeto da Engenharia de Reservatório /Unicamp /FINEP /CNPQ /PRONEX e a CAPES/ANP pela concessão de bolsa de estudos.

Aproximações quadráticas de ondas convertidas.

Coeficiente R_{sp}

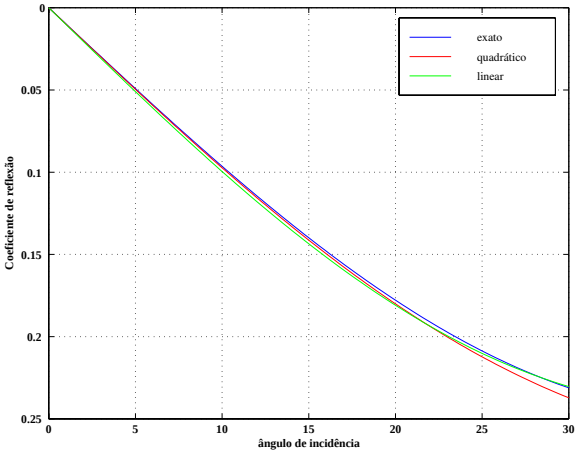

Figura 1: modelo folhelho/arenito

Coeficiente R_{sp}

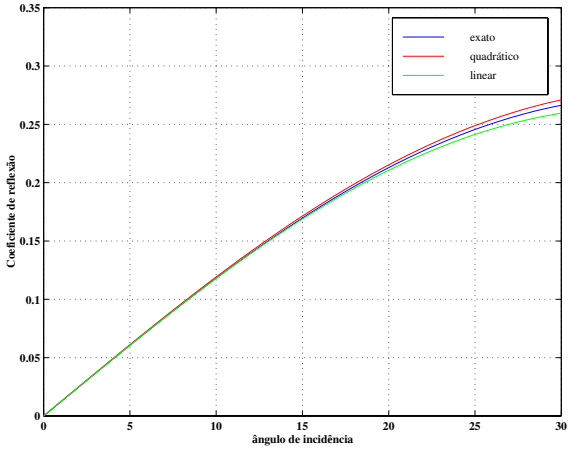

Figura 3: modelo anidrito/calcário

Coeficiente T_{sp}

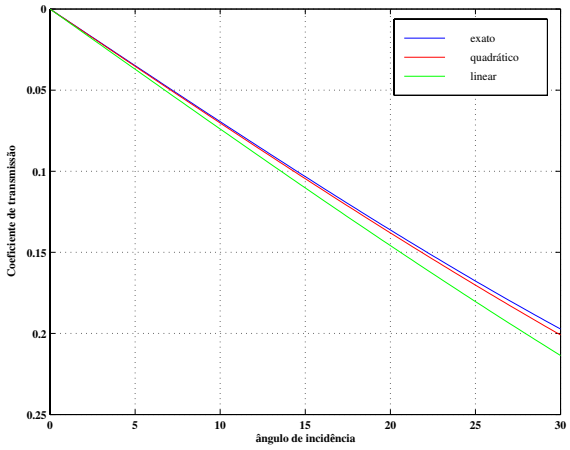

Figura 2: modelo folhelho/arenito

Coeficiente T_{sp}

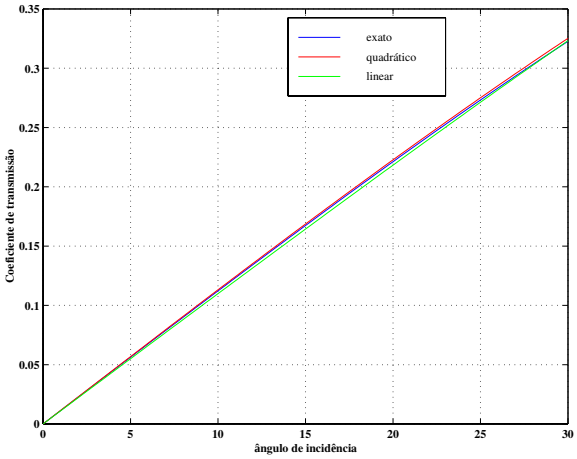

Figura 4: modelo anidrito/calcário

Combining P-P and P-SV AVO to Improve Estimation of Elastic Parameters

Antonio C. Buginga Ramos, PETROBRAS S/A, Brazil

Abstract

Compressional wave amplitude-versus-offset analysis (AVO) is being widely used in different geological settings as a lithology indicator and also as a direct hydrocarbon indicator. Ambiguities associated to elastic parameters estimation from AVO is commonplace in most inversion procedures used up today. Basic approaches to determine elastic parameters directly from the coefficients of the P-P reflectivity approximation (R_{pp}) fail because of the uncertainties associated to the third coefficient, which depend on larger incidence angles than intercept (*A*) and gradient (*B*) estimates. One way to get around this problem is to use the reflectivity information from P-SV AVO (R_{ps}) in addition to the traditional P-P AVO. This procedure can potentially reduce the uncertainties and improve estimation of elastic parameters.

In this paper I demonstrate how to extract elastic parameters from P-SV AVO and the way to combine these parameters with those extracted from P-P AVO. A simple low-contrast approximation is derived and is compared with a more accurate, yet more complex, high-contrast approximation. This procedure makes possible to access the uncertainties associated with the parameters estimated from P-SV AVO.

Introduction

Conventional P-P amplitude-versus-offset (AVO) analysis is an important exploration tool that exploits offset dependent P-wave reflectivity associated with hydrocarbons or lithology variations. It seems intuitive that converted wave P-SV AVO may provide useful complementary information to that obtained from P-P AVO analysis. With the development of ocean bottom cables, which include multicomponent seismometers, there is now more opportunity for the use of P-SV AVO technology. Here I will discuss a methodology to accomplish this combination, under assumption of isotropic media.

Near vertical incidence P-SV reflectivity is very small, since little conversion occurs at these angles. Typically the top of a class III reservoir (Rutherford and Williams, 1989) is characterized by strong negative P-P amplitude, which increases in magnitude with incidence angle. The same interface in the P-SV AVO generally exhibits positive amplitudes, which also increases in magnitude with incidence angle (upper curves in Figure 1a). In contrast, shale over brine sand interfaces, with increase in S-wave velocity and density in the brine sand with respect to the shale, normally exhibit negative P-SV amplitudes, with increase in magnitude with incident angle (lower curves in Figure 1b). This simple yet distinctive behavior demonstrates that P-SV AVO provides additional information to the traditional AVO technique, reducing the degree of uncertainty associated with velocities and density estimations.

Computation of P-P and P-SV reflectivity through exact Zoeppritz solvers offer very little in terms of physical insight into the problem. Reduction of the reflectivity problem to two or three coefficients approximations makes possible the construction of attribute traces directly and also allow the geophysicist to explore the powerful features of the AVO crossplot analysis.

Converted–wave P-SV AVO behavior may be fit with a cubic relationship between reflection coefficient and ray parameter. Attributes extracted using this form can be directly related to elastic parameters with low-contrast or high-contrast approximations to the Zoeppritz equations. The high-contrast approximation has greater accuracy, but it is a lot more complex than the analytically simple low-contrast approximation.

The low-contrast approximation for R_{ps}

Aki and Richards (1980) give a useful approximation for the P-SV reflection coefficient problem, which is given by:

$$R_{PS}(\theta) \approx -\left(\frac{1}{\cos\phi}\frac{\Delta\rho}{\rho} + \cos\theta\ 2\frac{\beta}{\alpha}\frac{\Delta\rho}{\rho} + \cos\theta\ 4\frac{\beta}{\alpha}\frac{\Delta\beta}{\beta}\right)\frac{\sin\theta}{2} + \left(\frac{\alpha\beta^2}{\cos\phi}\frac{\Delta\rho}{\rho} + \frac{2\alpha\beta^2}{\cos\phi}\frac{\Delta\beta}{\beta}\right)\frac{\sin^3\theta}{\alpha^3} \quad . \qquad (1)$$

In equation (1) α and β are the average P- and SV-wave velocities of the two media respectively, θ and ϕ are the average angles of incidence and refraction of the P- and SV-wave, respectively, and $\Delta\alpha/\alpha$, $\Delta\beta/\beta$ and $\Delta\rho/\rho$ are the fractional changes in P- and S-wave velocities and density across the interface, respectively. Equation (1) can be further simplified by making the following substitutions:

$$\cos\theta \approx 1 - \frac{\sin^2\theta}{2} \quad ,$$

and

$$\frac{1}{\cos\phi} \approx 1 + \frac{\beta^2}{2\alpha^2}\sin^2\theta \quad .$$

Now, collecting the powers of $\sin\theta$, one gets:

$$R_{PS}(\theta) \approx A_2 \sin\theta + B_2 \sin^3\theta + C_2 \sin^5\theta \ , \quad (2)$$

where :

$$A_2 = -2\frac{\beta}{\alpha}\frac{\Delta\beta}{\beta} - (\frac{1}{2} + \frac{\beta}{\alpha})\frac{\Delta\rho}{\rho} \ , \quad (2a)$$

$$B_2 = (\frac{2\beta^2}{\alpha^2} + \frac{\beta}{\alpha})\frac{\Delta\beta}{\beta} + (\frac{3}{4}\frac{\beta^2}{\alpha^2} + \frac{\beta}{2\alpha})\frac{\Delta\rho}{\rho} \ , \quad (2b)$$

$$C_2 = \left(\frac{\beta}{\alpha}\right)^4 \frac{\Delta\beta}{\beta} + \frac{1}{2}\left(\frac{\beta}{\alpha}\right)^4 \frac{\Delta\rho}{\rho} \ . \quad (2c)$$

Disregarding the fifth power of $sin\theta$, which is small for incidence angles below 30 degrees, I obtain a simple low-contrast, two-coefficient, approximation for *P-SV* reflection coefficient:

$$R_{ps}^{[2]}(\theta) \approx A_2 \sin\theta + B_2 \sin^3\theta \ . \quad (3)$$

The superscript and subscripts in equation (3) help to differentiate the low-contrast and the high-contrast approximation. The latter was derived expanding the angular dependencies in the exact R_{ps} equation in Taylor series and making no assumptions on small density and velocity contrasts. I used the high-contrast approximation (not shown here) to access the limitations of the simpler and more convenient low-contrast approximation (3).

As shown in equations 2a and 2b, the two coefficients of the low-contrast approximation (A_2 and B_2) are a function of the average ratio of compressional-to-shear-wave velocity (α/β) and the fractional changes in S-wave velocity and density ($\Delta\beta/\beta$ and $\Delta\rho/\rho$). Because of its simplicity, the low-contrast approximation is subject to errors, particularly for large positive contrasts in P-wave velocity associated with negative contrasts in S-wave velocity. However, for incidence angles up to 40 degrees and models confined to $|\Delta\beta/\beta|<0.25$, the errors in both coefficients are relatively small.

Comparison of approximations

Figures 1a and 1b show the variations of P-SV reflectivity with incidence angle for models 1 and 2 shown in Table 1 (modified from Castagna and Smith, 1994), which are typical shale / gas sand / shale and shale / brine sand / shale models. In these figures the high-contrast approximation and the low-contrast approximation are compared with the exact R_{ps} equation and its two-coefficient cubic fit, of the type: $A\ sin\theta_1 + B\ sin^3\theta_1$, where θ_1 is the incidence angle. The cubic equation fits the exact equation quite well in most cases and the high-contrast approximation is closer to the exact equation than the low-contrast equation (3). The magnitudes of the contrasts in elastic properties are: $|\Delta\alpha|$=0.23 km/s, $|\Delta\beta|$=0.09 km/s, $|\Delta\rho|$=0.15 g/cm^3, for Figure 1a, and $|\Delta\alpha|$=1.15 km/s, $|\Delta\beta|$=0.91 km/s, $|\Delta\rho|$=0.36 g/cm^3, for Figure 1b. The low-contrast approximation works relatively well in Figure 1a, a typical class III reservoir, where S-wave velocity contrast is small, and both A_2 and B_2 have the same sign.

In Figure 1b the contrasts in elastic properties are large, which tends to make the low-contrast approximation poor. There is a significant change in both P- and S-wave velocities. However, only when the changes in P- and S-wave velocities are positive (shale over brine sand case) there is a significant difference between the high- and low-contrast approximations and the exact equation. This difference is mostly due to the error in B_1 and B_2 (second coefficients of the high- and low-contrast approximations respectively).

The A_2 coefficient of the low-contrast approximation is well constrained and is generally very similar to the A_1 coefficient of the high-contrast approximation. In fact, if the contrasts in P- and S-impedances of both media are small, one can prove that A_2 becomes approximately A_1.

Model	Rock	α (km/s)	β (km/s)	ρ (g/cm^3)
1	shale	3.27	1.65	2.20
1	Gas sand	3.04	1.74	2.05
2	shale	2.31	0.94	1.90
2	Brine sand	3.46	1.85	2.26
3	Shale	2.31	0.85	2.18
3	Brine sand	2.52	0.90	2.11

Table 1 – Elastic properties used in Figures 1 and 2.

Obtaining parameters from P-SV AVO

Assuming that A_2 and B_2 can be measured from the P-SV AVO and α/β ratio can be roughly estimated from logs and P-P-wave AVO, one obtain (using equations 2a and 2b):

$$\frac{\Delta\rho}{\rho} = -\frac{2\left[(2\frac{\beta}{\alpha}+1)\ A_2 + 2\ B_2\right]}{(\frac{\beta}{\alpha}+1)^2} \ , \quad (4)$$

$$\frac{\Delta\beta}{\beta} = \frac{\left[(\frac{\beta}{\alpha}+\frac{3}{2}\frac{\beta^2}{\alpha^2})\ A_2 + (2\frac{\beta}{\alpha}+1)\ B_2\right]}{\frac{\beta}{\alpha}(\frac{\beta}{\alpha}+1)^2} \ . \quad (5)$$

Obtaining parameters from P-P AVO

Exact P-P reflection coefficient is also given by the well-known Zoeppritz, which is expressed by a complicated function of elastic parameters and angles of incidence and refraction. For moderate angles of incidence and small contrasts in elastic properties, the P-P AVO may be simplified to a linearized approximation with three coefficients (Swan, 1993):

$$R_{pp}(\theta) \approx A + B\sin^2\theta + C\sin^2\theta\tan^2\theta, \quad (6)$$

where

$$A = \frac{1}{2}\left(\frac{\Delta\alpha}{\alpha} + \frac{\Delta\rho}{\rho}\right), \quad (6a)$$

$$B = \frac{1}{2}\frac{\Delta\alpha}{\alpha} - 2\left(\frac{\beta}{\alpha}\right)^2\left(2\frac{\Delta\beta}{\beta} + \frac{\Delta\rho}{\rho}\right), \quad (6b)$$

$$C = \frac{1}{2}\left(\frac{\Delta\alpha}{\alpha}\right) \quad (6c)$$

Combining the coefficients of equations 6a through 6c one obtain the following estimates of elastic parameters:

$$\frac{\Delta\rho}{\rho} = 2\,(A - C), \quad \text{and} \quad (7a)$$

$$\frac{\Delta\beta}{\beta} = \frac{(C-B)}{4\left(\frac{\beta}{\alpha}\right)^2} + (C - A). \quad (7b)$$

By making a simple substitution of $\tan\theta$ by $\sin\theta/\cos\theta$ in equation 6, one obtain a quadratic equation in $\sin\theta$, therefore the *C* term represents a quartic slope, which is highly sensitive to noise and velocity errors in the overburden (Swan, 1993).

Discussion

The estimated parameters $\Delta\beta/\beta$ and $\Delta\rho/\rho$ should be affected when gas replaces the liquid phase in a porous sandstone reservoir encased in shales. Figure 2 shows the variation in these parameters as gas replaces water in the sand (properties for 100% water saturation are shown in model 3 of Table 1). In this case, as gas saturation increases, the sand becomes a class III reservoir, $\Delta\beta/\beta$ becomes more positive and $\Delta\rho/\rho$ becomes more negative. This is due to the fact that gas reduces the density of the sandstone, which causes increase in its S-wave velocity. Conversely, the presence of gas in the sand initially causes a large drop, and change in sign, of $\Delta\alpha/\alpha$. As water saturation is further decreased, the magnitude of $\Delta\alpha/\alpha$ does not change significantly. The behavior of a class IV reservoir is slightly different since $\Delta\beta/\beta$ is negative for 100% water saturation and decreases its magnitude (becoming less negative) as gas replaces water in the reservoir. However, similarly to the class III sand, $\Delta\rho/\rho$ is negative for the brine case and becomes more negative as water saturation is decreased. Therefore the fractional change in density decreases in magnitude as gas saturation increases in both cases of class III and IV reservoirs.

As demonstrated in equations 7a and 7b, estimation of $\Delta\rho/\rho$ and $\Delta\beta/\beta$ from P-P AVO depend on the worst determined quartic coefficient *C*, which greatly depend on the correctness of the background velocity model. Estimating $\Delta\alpha/\alpha$ is possible through equation 6c. In this case, however, there is a dependency on the *C* term of R_{pp} approximation, which substantially increases the uncertainties of $\Delta\alpha/\alpha$.

The parameter $\Delta\beta/\beta$ determined from P-SV AVO (5) becomes important when compared to the P-P AVO intercept (6a), which essentially retains the changes in fluid properties in $\Delta\alpha/\alpha$ and $\Delta\rho/\rho$. The analysis of sections formed by all three elastic parameters ($\Delta\alpha/\alpha$, $\Delta\beta/\beta$ and $\Delta\rho/\rho$) may help distinguish full from partial gas saturation (Figure 2).

The correctness of the B_2 coefficient (2b) of the low-contrast approximation is addressed when this coefficient is compared with the second coefficient obtained from cubic fit to the exact equation. When one considers a large number of possible exploration models it is apparent that for $|\Delta\beta/\beta| < 0.25$, the errors in the B_2 coefficient are relatively small.

While the expression of B_2 (low-contrast approximation) can be described by a simple function of three parameters: $\Delta\beta/\beta$, $\Delta\rho/\rho$ and β/α (equation 2b), the expression of B_1 (high-contrast approximation) is a complicated equation involving different combinations of α, β and ρ for each medium. B_2 clearly does not depend on $\Delta\alpha/\alpha$, while the exact equation and the high-contrast approximation do. Therefore, part of the error associated with B_2 can be explained by its complete independence of $\Delta\alpha/\alpha$.

The A_2 coefficient (2a) from the low-contrast approximation is a much better constrained parameter than the B_2 coefficient (2b). This suggests that the best combination of coefficients to estimate elastic parameters should be the one involving A_2 from P-SV AVO and *A* and *B* from P-P AVO. With these three equations all three elastic parameters ($\Delta\alpha/\alpha$, $\Delta\beta/\beta$ and $\Delta\rho/\rho$) can be estimated.

Conclusions

Combination of P-P and P-SV AVO analysis provides a relatively robust approach for estimating elastic parameters directly from the coefficients of R_{pp} and R_{ps} approximations. Together the parameters estimated from this AVO combination may provide improved direct hydrocarbon indication and can potentially be used to identify anomalies caused by low gas saturations.

References

Castagna, J. P. and Smith, S. W., 1994, A comparison of AVO indicators: A modeling study: Geophysics, 59, 12, 1849-1855.

Ramos, A. C. B., and Castagna, J. P., 2001, Useful approximations for converted wave AVO, Geophysics, submitted for publication.

Rutherford, R.S., and Williams, R. H., 1989, Amplitude-versus-offset variation in gas sands: Geophysics, 54, 680-688.

Swan, H.W., 1993, Properties of Direct AVO Hydrocarbon Indicators, in Castagna, J. P. and Backus, M. M., Eds., Offset Dependent Reflectivity – Theory and practise of AVO analysis, Soc. Expl. Geophys., 333-345.

Acknowledgments

I would like to thank PETROBRAS for permission to publish this work.

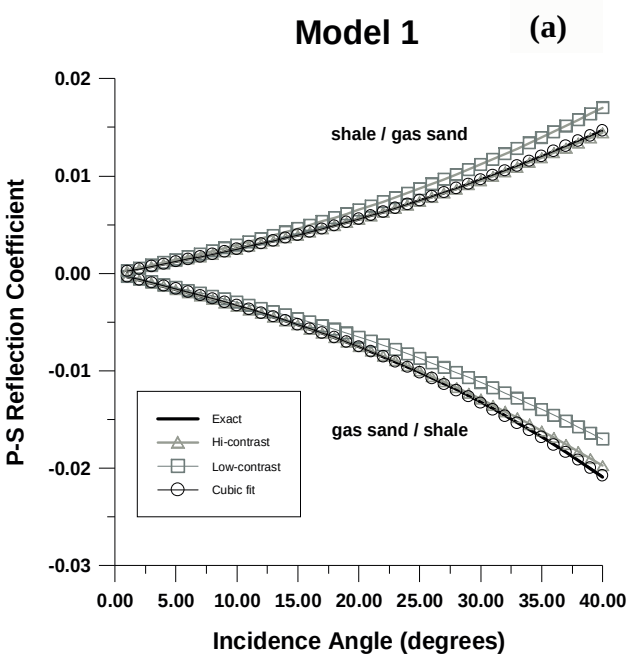

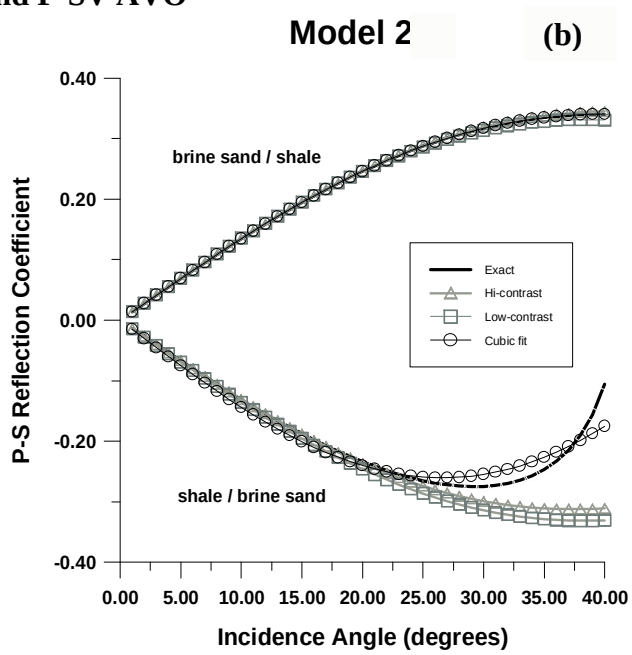

Figure 1- Non-normal P-SV-wave reflectivity responses (R_{ps}) for the models presented in Table 1. Notice the better agreement between approximations and exact R_{ps} for model 1 (a) and the brine sand over shale of model 2 (b).

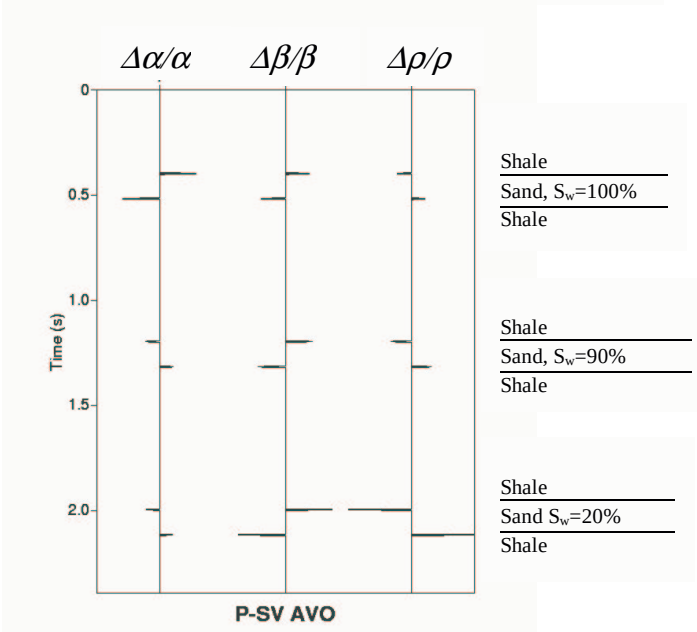

Figure 2 – Attributes $\Delta\alpha/\alpha$, $\Delta\beta/\beta$ and $\Delta\rho/\rho$ for three different water saturations (S_w) indicated in the figure. Brine reservoir properties are from model 3 (Table 1). Notice the opposite behavior of $\Delta\alpha/\alpha$ and $\Delta\beta/\beta$ as we move from a water sand (top) to a gas sand (bottom). In this case, low gas saturations can be distinguished from high gas saturations from the magnitudes of $\Delta\beta/\beta$ and $\Delta\rho/\rho$ with respect to $\Delta\alpha/\alpha$..

Determination of Reservoir Characteristics by Multiple Diffraction Stacking (MDS)

J. C. R. Cruz, G. Garabito and K.A.Obaidullah.
jcarlos@ufpa.br, german@ufpa.br, ahmedi@ufpa.br

Abstract
Amplitude-versus-offset or (AVO) analysis is usually carried out by using linear approximations of the Knott-Zoeppritz equation. For comprehensive analysis, a detailed knowledge of velocity model is essential to determine incidence angles using ray tracing. The angular reflection coefficients and the incidence angles are determined by means of double-diffraction stack of common-offset seismic data. For determining zero-offset reflection coefficients is used a true amplitude Kirchhoff migration operator. The two resulting sets are then used in Hilterman's linear approximation of Zoepritz Equations to determine NI and PR. As long as we are within the bounds of assumptions involved, a reasonable estimate of the zero-offset reflection coefficient or the Poisson reflectivity can be made. The data sets of the two parameters are then available for attribute determination and reservoir characterization.

Introduction
Amplitude-versus-Offset (AVO) analysis is an established technology for reconnaissance and detailed reservoir studies. The methods use linear approximations of the Knott-Zoeppritz equations, on the assumptions of small changes across interfaces. Castagna and Backus (1993) review underlying theoretical basis, and some early applications. In particular approximation, Verm and Hilterman (1995) give normal incidence reflectivity (NI) and Poisson's reflectivity (PR) provided detailed velocity model is available for determining the incidence angles.
We present a method for determining the two AVO parameters without resorting to modeling. Instead the incidence angles are determined by means of double-diffraction stack of common-offset seismic data.

Procedure of determining NI and PR:
The following three steps are required to determine NI and PR: (1) Determination of angle-dependent reflection coefficient by means of true-amplitude Kirchhoff migration; (2) Determination of incidence angle by means of double-diffraction stack; (3) By combining the first two steps with Hilterman's formulas we determine the NI and PR reservoir parameters.

True-Amplitude Migration
The 2-D true-amplitude migration uses the following two dimensional diffraction stack operator

$$V(M,t) = \frac{1}{\sqrt{2\pi}} \int_A d\xi w(\xi, M) \partial_{t-}^{1/2} U(\xi, t+\tau_D) \quad (1)$$

given by Urban (1999) based on Schleicher et al. (1993). In the equation (1), the source and receiver pairs (S, G) are parameterized by variable ξ, in such way that the diffraction in-plane traveltime curve τ_D is defined for all points of parameter ξ on the earth surface, and a point M within a specified volume of the seismic model. The symbol $\partial_{t-}^{1/2}$ is the anti-causal half-time derivative operator that corresponds in the frequency domain to the filter ($\sqrt{i\omega}$). The weight function w is chosen so that the result of migration process is proportional to the angle-dependent reflection coefficient. The function $U(\xi, t + \tau_D)$ represents the principal component of the seismic primary reflected wavefield. The result of the integral (1) is put at the point M into the model, providing what we call true amplitude diffraction stack migration. The half derivative filter is applied in frequency domain. The appropriate weight function is calculated and applied to the amplitudes. The resulting section, gives the reflection coefficient at each reflection point in depth model.

Incidence Angle Determination
Based on the Born and ray theoretical approximations, Bleistein (1987) and Tygel et al. (1993), respectively, presented a new inversion method, the so-called Double Diffraction Stack (DDS). By this method it is possible to estimate several parameters of a selected ray between the source and geophone at any arbitrary configuration of the seismic data. This inversion technique is based on the weighted diffraction stack integral, which is used above for migration. Alternatively, we write $V(M,t)=V_j(M,t)$, where j is the index of the weight to stack the seismic data. The DDS inversion technique is then done by a double stack, each one with a different weight function j = 1 and j = 2. The result is obtained by the ratio between the two stacks given by

$$V_{DDS}(M,t) = \frac{V_1(M,t)}{V_2(M,t)} \quad 2$$

considering a high frequency solution of the stationary phase method applied to the stack integral operators.
In this paper, we have used in V_1, as weight function, the half angle between the ray trajectories from a point M in depth to the source and geophone positions at the earth surface. If M is a reflection

point the weight equals the incidence angle. By using as input a set of common-offset seismic section, we have the incidence angle signed to each reflection point in the subsurface.

It is an inversion technique represented by equation (2), where the weight function is defined twice, first as the half angle between the source and geophone ray trajectories, through the point M in depth, and second as the unity. By dividing the results of the two stack process with their respective weight functions, we obtain the incidence angles at the reflection points. For avoiding division by zero, we consider a minimum value in the denominator.

NI and PR Determination

Amongst the several approximations of the Zoeppritz equations, Verm and Hilterman (1995) give the form

$$RC(\theta) = NI\cos^2\theta + PR\sin^2\theta \qquad (4)$$

The parameters NI and PR are the normal incidence and Poisson reflectivity, respectively. These parameters relate to reservoir properties. The Equation (4) can be rewritten as follows

$$RC(\theta) = NI + (PR-NI)\sin^2\theta \qquad (5)$$

In Equation (5), the intercept gives the NI and the slope of a plot of $RC(\theta)$ versus $\sin^2\theta$ allows the determination of PR.

Example of Application

The NI, PR determination has been tested on a depth model of one layer over a half space. The top layer with a velocity (V_1) given by $V_1 = 1800 + .365Z$ m/s. The half space has a constant velocity of 4500 m/s. The velocities satisfy Hilterman's approximation requirements. In Figure 1b shows the seismic model with rays for a common-offset of l000m; and Figure 1a the corresponding synthetic seismogram generated by using the SEIS88 ray package. Figure 2a shows a plot of angular reflection coefficients versus midpoint theoretical and estimates obtained by the true-amplitude migration process. The angular reflectivity estimates closely follow the theoretical curve, except at the boundaries due to incomplete operator. The Figure 2b shows a plot of theoretical and estimates of the incidence angles using the double-diffraction stack method. These are plotted versus midpoint. The estimates follow the theoretical curve with reasonable accuracy.

In Fig.2c, the estimates of reflectivities at midpoint 2.75 Km are plotted against $\sin^2(\theta)$. The straight line is the curve of equation (5) which may also be considered as best fit for the estimated values. The intercept of the line gives the normal incidence reflectivity (NI) and from the slope we can obtain the Poisson Reflectivity (PR). Both these parameters are then available for further attribute analysis to characterize reservoir properties.

Conclusions

We have in this paper presented a new method for determining NI and PR parameters using the Hilterman's approximation formula, and a double diffraction stack algorithm.

We feel the method has application potential at the level of initial scanning of data for amplitude anomalies.

Acknowledgments

We thank the National Petroleum Agency of Brazil (ANP) for supporting two of the authors of this research, Prof. Dr. P. Hubral of Karlsruhe University, Germany and also the seismic work group of Charles University, Prague, Tchech Republic, for making the ray tracing software SEIS88 available to us.

4 (4)

References

Aki, K., and Richard, P., 1980, Quantitative seismology: theory and methods, volume 1 W.H. Freeman and Co., 1 edition..

Bleistein, N., 1987, On the imaging of reflectors in the earth: Geophysics, 52, 931-942.

Castagna, J., and Backus, M., 1993, Offset-dependent reflectivity - theory and practice of avo analysis, number 8 in investigations in geophysics SEG.

Schleicher, J., Tygel, M., and Hubral, P., 1993, 3-D true-amplitude finite-offset migration Geophysics, 58, 1112-1126.

Tygel, M., Schleicher, J., Hubral, P., and Hanitzsch, C., 1993, Multiple weights in diffraction stack migration: Geophysics, 57, 105-1063.

Urban, J., 1999, True-amplitude migration in bi-dimensional media and introduction to the 2.5-d case, in portugese: Master's thesis, Federal University of Para, Brazil.

Verm, R., and Hilterman, F., 1995, Lithology color-coded seismic sections: the calibration of avo crossplotting to rock properties: The Leading Edge, 14, no.8, 847-853.

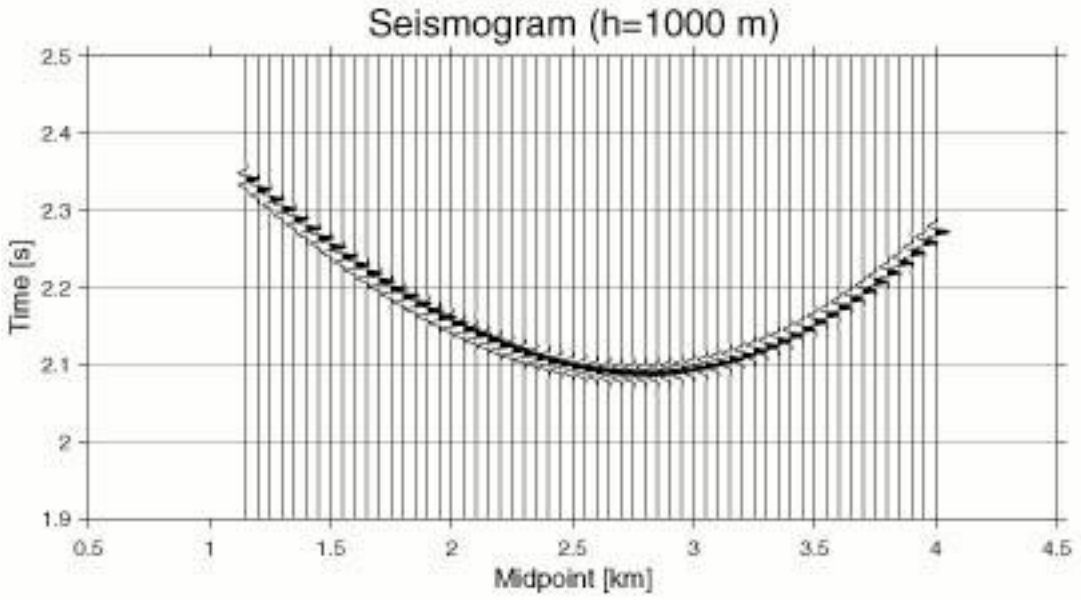

(a)

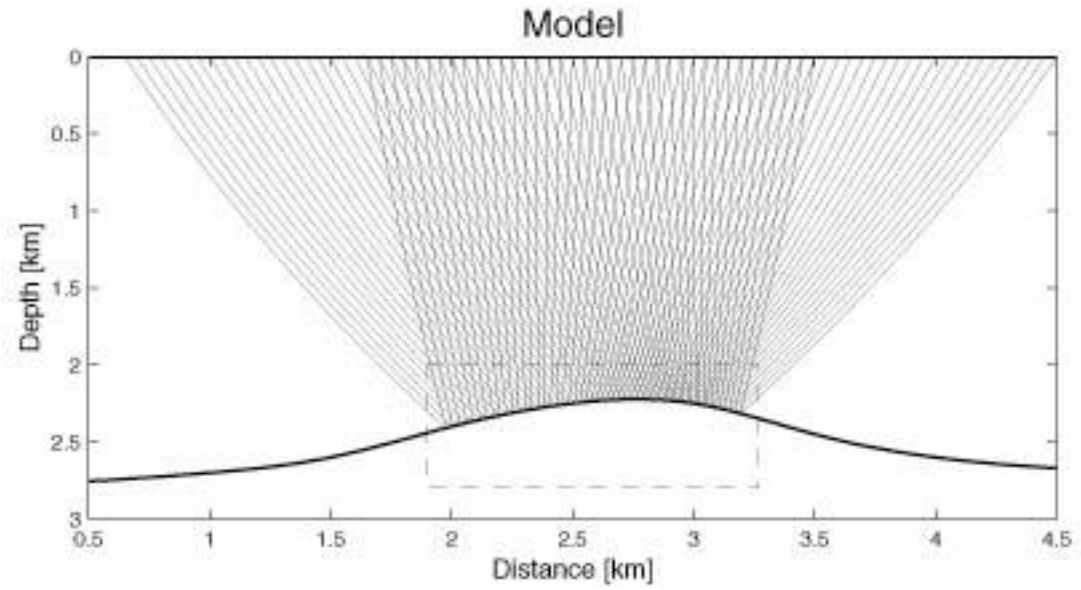

(b)

Figure 1. (a) Synthetic constant offset section generated by ratracing package SEIS88 for 1000m offset for the model in (b). **(b)** Elastic model of reservoir represented by a constant gradient velocity layer above a constant velocity half-space.

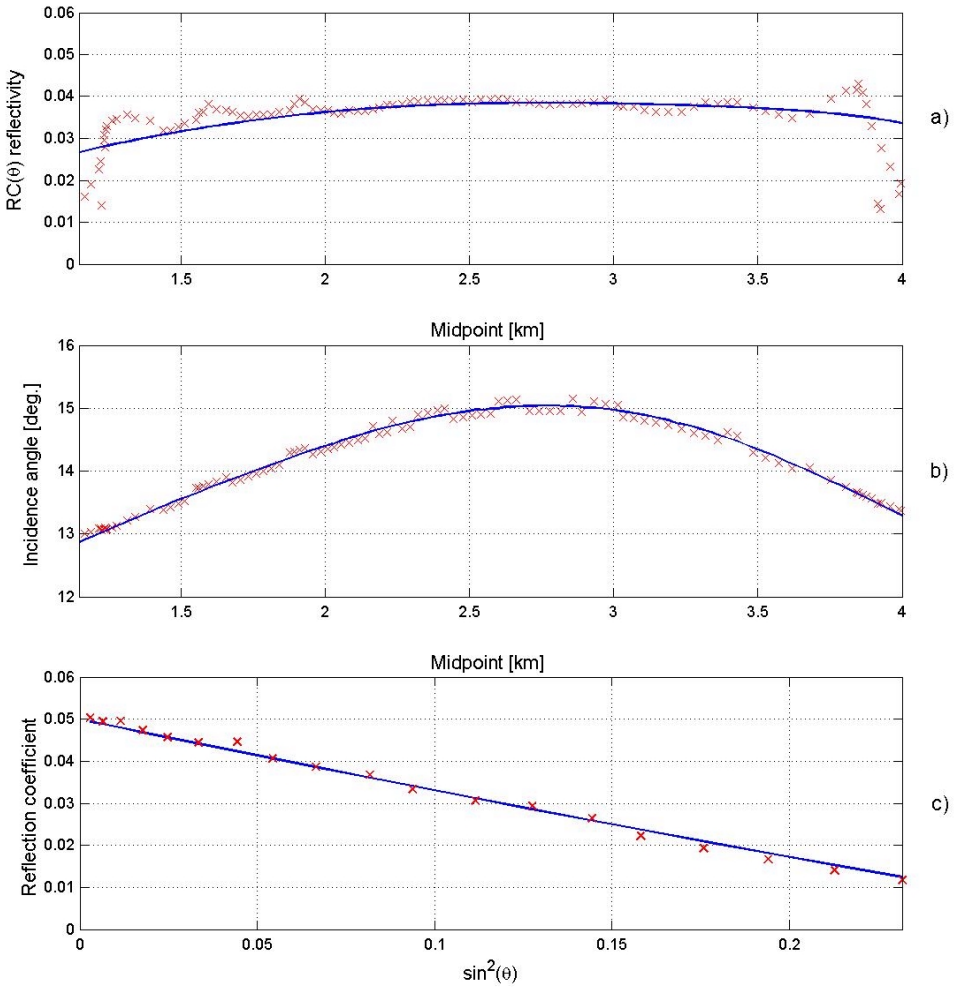

Figure 2. (a) Angular reflectivity theoretical (solid line) and estimated; **(b)** Incidence angle theoretical (solid line) and estimated; **(c)** plot of reflectivity versus sine square of incidence angles theoretical (solid line) and estimated.

Interpretation of Long Offset AVO Attributes

Douglas Foster, Phillips Petroleum,

Jeff Malloy, Phillips Petroleum

Bill Beck, Phillips Petroleum

Marc Sbar, Phillips Petroleum

Abstract

AVO effects in large offset P-wave data (up to 60°) is investigated. In addition to conventional P-wave AVO attributes (*A* and *B*) a third term (*C*) is examined. Background trends for crossplots of the attributes are related to rock property relationships. Exact expressions are given for the first 3 terms, (*A*, *B*, *C*), of the expansion of Knott-Zoeppritz equations of the reflected P-wave energy. These exact expressions are compared to the commonly used linearized (first order contrasts of rock properties) attributes. The effect of variation in water saturation and porosity in a sandstone embedded in shale is investigated in a numerical example, based on rock physics models of a well log. The AVO attributes show promise to distinguish so-called fizz-gas (low saturated gas sands) from commercial gas and differentiate porosity in reservoir rocks.

Introduction

Amplitude versus offset (AVO) analysis of seismic reflections has been used in hydrocarbon prospecting for over 20 years. Initially, AVO analysis was used for direct seismic detection of gas bearing sandstone sediments and highgrading "bright" amplitudes on conventional seismograms. In principle, AVO analysis can resolve some of the ambiguity of lithological and hydrocarbon "bright" amplitudes. Since then other applications, such as oil versus gas discrimination, lithology prediction, and "nonbright" hydrocarbon reflections, have been reasonably successful.

Typically, the interpretation of an AVO anomaly incorporates two attributes. The most common AVO attributes are the zero offset reflectivity, or intercept (*A*), and the slope (*B*) of the reflection amplitude as a function of $\sin^2(\theta)$, where θ is the incidence angle. For relatively short offsets (up to 30° of the incident angle), *A* and *B* accurately approximate the reflection coefficient. Also, these two parameters relate the reflection coefficient to the density (ρ), and to compressional (α) and shear (β) velocities of the overlying and underlying media of a reflective interface.

In recent years exploration seismic surveys are being recorded with longer streamers (i.e. 6 km. and greater). Shuey, (1985) and Aki and Richards, (1980) approximations are based on the assumption that a linear relation between the reflection coefficient and $\sin^2(\theta)$ exists for angles of incidence less than 30°. There is an additional assumption that rock property contrasts are relatively small (first order approximation). Using long streamers can provide data up and beyond angles of incidence up to 60°, so clearly the small angle approximation is not valid. In addition, elastic properties and density can be distinctly different from the surrounding strata, therefore a first order approximation may not be adequate particularly at far offsets.

Given these new types of data, we will propose how to interpret these types of data in terms of rock and fluid properties. Foster et al., (1997) showed an approach to obtain AVO attributes, *A* and *B*. A similar approach is given by Ursin and Dahl (1992). This approach avoids the small contrast approximation and allows any rock property contrast. In this paper, we analyze long offset P-wave data using a three term expansion, *A, B,* and *C*. Also, we examine the differences of the more conventional (first order) attributes and the exact ones (for any contrasts) proposed by Hansen (2001).

Theory

Contrary to the first order approximation to equations used by Aki and Richards, (1980) and Shuey, (1985), the Zoeppritz equation can be expanded with respect to $\sin^2(\theta)$. *A* and *B* are obtained using the first two terms of the compressional wave reflection coefficient (R_{pp}) expansion around $\sin^2(\theta) = 0$. This approach allows arbitrarily large changes in the elastic parameters α, β, and density, ρ, across interfaces. We extend this to incorporate the third term, *C*. The expansion of R_{pp} is

$$R_{pp}(x) = A + Bx^2 + Cx^4 + O(x^6), \qquad (1)$$

where, $x = \sin(\theta)$.

For relatively small contrasts in velocity and density coefficients in Equation 1 may be approximated by (Aki and Richards, 1980)

$$A = \Delta\alpha/2\alpha + \Delta\rho/2\rho, \qquad (2)$$

$$B = \Delta\alpha/2\alpha - 4\gamma^2(\Delta\rho/2\rho + \Delta\beta/2\beta), \qquad (3)$$

and

$$C = D\alpha/2\alpha. \qquad (4)$$

In equations (2), (3), and (4), α, β, ρ, and g are the average compressional velocity, shear velocity, density, and the shear to compressional velocity ratio above and below the reflecting interface; $D\alpha$, $D\beta$, and $D\rho$ are the differences of the rock properties between the layer below and the layer above the reflector.

Neglecting second order terms,

$$Dg/g = D\beta/\beta - D\alpha/\alpha. \qquad (5)$$

Substituting equation (5) into (2) and (3) shows that

$$B = (1 - 8^2)A - 4gDg + (4^2 - 1)D\rho/2\rho. \qquad (6)$$

Equations (2) and (4) give

$$C = A - D\rho/2\rho. \qquad (7)$$

Crossplotting of AVO attributes has been proven a valuable tool. In a conventional crossplot of *A-B*, a background trend can be observed for non-hydrocarbon bearing lithologies, depending on the $g = \beta/\alpha$ ratio, This *A* and *B* trend comes from the relationship of $\acute{a}$ and $\hat{a}$.

Background Trends

Castagna et al., (1985) observe that in nonhydrocarbon bearing rocks, the shear wave velocity is approximately a function of the compressional wave velocity. Also, in the absence of hydrocarbons, well logs routinely show that g slowly varies over large intervals in clastic sediments particularly in shales. When hydrocarbon bearing rocks are encountered there is no correlation between $\acute{a}$ and $\hat{a}$. In hydrocarbon bearing rocks, $\acute{a}$ is strongly affected but the effects on $\hat{a}$ are minimal. Points anomalous to the background trend in the *A-B* crossplot are a result of a change in $\tilde{a}$ which can be due to the presence of hydrocarbons. Figure 1 summarizes the interpretation of the *A-B* crossplot.

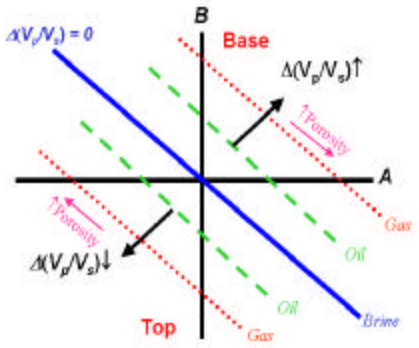

Figure 1. Background trends for the *A-B* crossplot are shown for a range of values for g.

The crossplot of *A* and *C* can be interpreted in two ways. One interpretation exploits equation (7) and shows that when density is constant, then *A* = *C*. There is no dependence on the g. Figure 2 shows how the *A-C* crossplot is interpreted using first order AVO attributes.

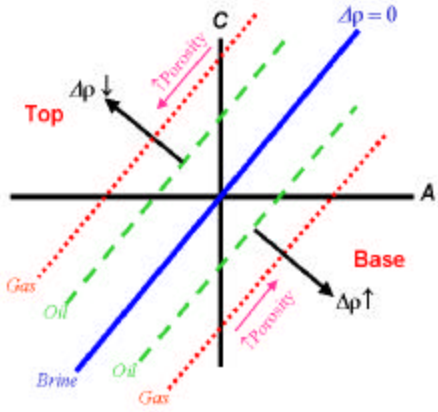

Figure 2. Background trends for the *A-B* crossplot are shown for a range of values for g.

A reasonable simplification to investigate the properties of the background trend, i.e. when no hydrocarbons are present, is that a change in the β/α ratio is small ($Dg = D(\beta/\alpha) \gg 0$), and that variation in density is small ($D\rho \gg 0$). This simplification leads to the following background trends (*B/A* from Foster et al., 1997, and *C/A* from Hansen et al. 2001)

$$B = (1 - 8^2)A + O(A^2),$$

and

$$C = (1 + 2\gamma^3 - 2\gamma^5)A + O(A^2).$$

The background trends for various values of γ are plotted in Figures 3 and 4. We see that the slope of the background trend in the *A-B* plane is very dependent on . Small changes in will lead to significant changes in slope. The background trend in the *A-C* plane has a slope of 1.2 and a slope of -1.0 in the *A-B* plane, almost independently of .

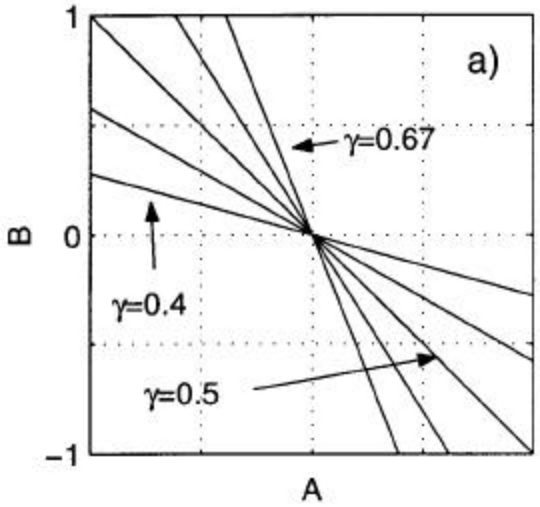

Figure 3. Background trends for the *A-B* crossplot are shown for a range of values for γ

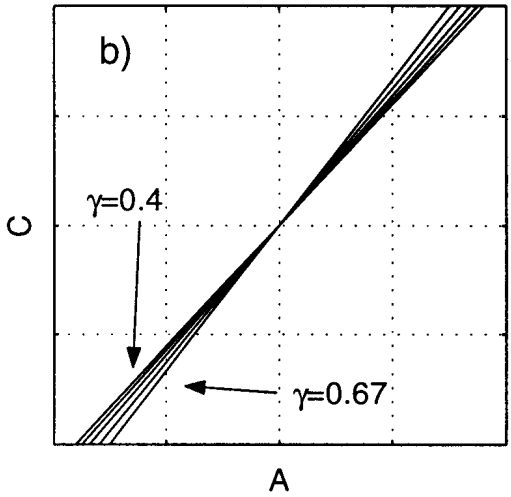

Figure 4. Background trends for the *A-C* crossplot are shown for a range of values for γ

Since these background trends are approximately linear, the higher order terms can be significant. Foster et al. (1997) show the background trend of *A* and *B* is exactly linear if and only if the background β/α = 1/2. In a similar way it is likely that the *A-C* trend is also dependent on the background γ. One advantage of using these attributes is if one starts with first order attributes (i.e. Aki and Richards) a linear relationship between α and β can only lead to a linear relationship between the attributes. Although first order attributes may accurately model the reflection coefficients as a function of offset, they cannot provide insight into the higher order relationship to the background rock property relationships.

The *A-B* and *A-C* crossplots for models with varying water saturation, S_w are shown in Figures 5 and 6. The small dots around the background trend are the calculated exact AVO attributes derived from a well log. These plots show the exact A is closely approximated by the first order A however the error in B and C grows increasingly.

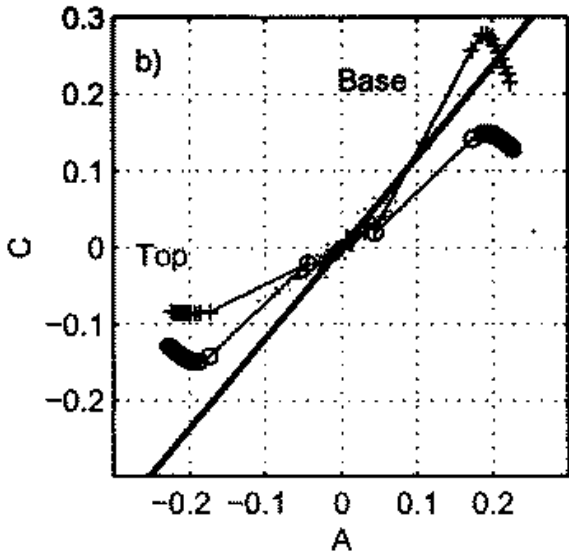

Figures 5 shows the *A-C* crossplot for variable water saturation. Circles (o) are Aki and Richards AVO attributes, and crosses (+) are the exact AVO attributes. The solid line denotes the background trend for = 0.5

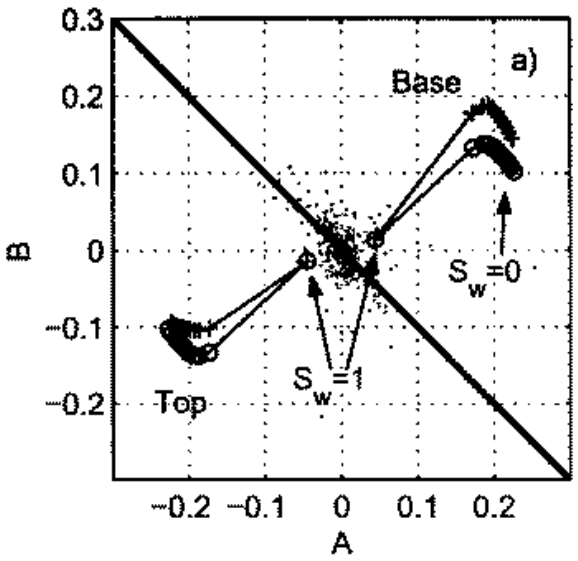

Figures 6 shows the *A-B* crossplot for variable water saturation. Circles (o) are Aki and Richards AVO attributes, and crosses (+) are the exact AVO attributes. The solid line denotes the background trend for = 0.5

Conclusions

Expanding the Knott-Zoeppritz equation for R_{pp} with respect to $sin^2(\theta)$, we have investigated the 3rd term in the Taylor expansion. There are differences between the exact coefficients and the first order Aki and Richards attributes. The approximate and exact *A* are similar but the approximate *B* shows significant error and *C* is worse. For P-wave data, there are indications that separation between gas- and fizz-gas bearing gas sands is enhanced in *A-C* cross plots, compared to the conventional *A-B* cross plot.

Acknowledgemenhts

We thank the Phillips Petroleum Corporation for their permission to publish these results. Also we acknowledge, Thomas Hansen, Robert Keys, and Chuan Yin.

References

Aki, K., and Richards, P.G., 1980, Quantitative seismology : Theory and methods, volume 1: W, H. Freeman and Co., San Fransisco.

Castagna, J.P., Batzle, M.L., and Eastwood, R.L., 1985, Relationships between compressional-wave and shear-wave velocities in clastic silicate rocks: Geophysics, **50**, no. 4, 571--581.

Foster, D.J., Keys, R.G., and Reilly, J.M., 1997a, Another perspective on AVO crossplotting: EdgeNET, http://www.edge-online.org, **9**, 1--4.

Foster, D.J., Keys, R.G., and Schmitt, D.P., 1997b, Detecting subsurface hydrocarbons with elastic wavefields: Chavent, H., Papanicolaou, G., Sacks, P., and Symes, W., Eds., Inverse Problems in Wave Propagation:: Springer, 195--218.

Hansen, T.M., Foster, D.J., and Hornby, B.E., 2001, AVO attributes of long offset P-waves and converted waves: submitted to Geophysics.

Shuey, R.T., 1985, A simplification of the Zoeppritz-equations: Geophysics, **50**, no. 4, 609--614.

Ursin, B., and Dahl, T., 1992, Seismic reflection amplitudes: Geophysical Prospecting, **40**, 483-512.

Quantifying AVO attributes and their effectiveness

Christopher P. Ross, Hampson-Russell Software, Houston, Texas, USA

Abstract

Quantifying the effectiveness of any AVO technique has always been a concern for progressive geoscientists assessing and modeling reservoirs. This paper compares three major AVO-based attributes and their applications. Elastic impedance, lambda-mu-rho, and conventional intercept-gradient AVO techniques are compared for various angular apertures and well availability using a 3D prestack seismic model. The effectiveness of each technique is determined by comparing the apparent reservoir extent to the known reservoir extent.

Introduction

Amplitude variation with offset techniques are used by exploration and production groups to assist in hydrocarbon location in clastic depositional settings. While exploration groups tend to use AVO attributes for detection and risk quantification, exploitation and production groups use AVO attributes for detection and reservoir characterization. Accurate geoscience and engineering characterization (parameterization) of the reservoir can result in accurate prediction of hydrocarbon reserves and effective production of the reservoir. It is therefore essential to understand what seismic attributes will best contribute to the characterization of the subsurface reservoir. This paper focuses on the accuracy of AVO attributes commonly used in reservoir characterization. In particular, the effectiveness of lambda-mu-rho, elastic impedance, and intercept-gradient AVO attributes, and their ability to accurately predict reservoir extent are presented.

One might argue (as does this author) that each of these three techniques is essentially the same, owing to the fact that each attribute set comes from the measurement of amplitude variation with offset across a velocity-corrected CMP gather. But some geoscientists prefer one attribute type over another, or logistically only have access to a certain attribute. This paper examines the differences between the methodologies of extracting the various attributes and more importantly, compares the final computed attribute answers. Please note that looking for the best AVO attribute for reservoir characterization does not mean that this attribute will be the sole seismological contribution to the reservoir parameterization for reservoir simulations, but rather a qualifier as to the best AVO input (if any) to accompany other geophysical and geological inputs to the modeling.

Methodology and testing

Data and modeling: Data models were constructed using well log data with fluid and thickness substitution techniques. For this example, the well log is from the middle Miocene section on the northern continental shelf area of the Gulf of Mexico. A thin, blocky sand encased by shales was selected as the reservoir, which when gas-saturated can be categorized as a class 2 AVO response. (The gas reservoir has a higher velocity and lower density than surrounding shales.) The model was constructed by seeding the reservoir thickness geometry with individual full-elastic wave equation synthetic seismograms with the selected cell thickness and fluid type. The resulting 35 inline by 50 crossline model contains two sands that vary in thickness from zero to 11 m at a depth of 2700 m (2.2 s), and the model is essentially devoid of structure. A zero-phase 4/8-24\48 Hz wavelet was used, and data was acquired to a maximum offset of 4900 m. Velocity information used for angle estimation and AVO gradient calculation came from a smoothed version of the initial sonic log, and a robust fit was used to eliminate outlying points in the gradient measurements.

Intercept-gradient (A-B) attributes: From the synthetic CMPs, sample-by-sample AVO gradient calculation was performed and AVO intercepts subsequently estimated. Three intercept and gradient sets were generated with maximum incident angles of 32, 40, and 48 degrees. The A-B attributes are the traditional “base” AVO attributes computed from CMP data.

Elastic impedance (AI-EI) attributes: The procedure to calculate these attributes involves computation of partial angle stacks, one near angle and one far angle stack, and inverting both for impedances. The near angle stack inversion is for acoustic impedance (AI), and the far angle stack inversion, termed by Connolly (1999), is for elastic impedance (EI). A constrained

Quantifying AVO Attributes

GLI inversion algorithm is used for all inversions and the inversion process begins with an initial impedance model constructed from well log impedances and seismic interpretation horizons (used to interpolate the interwell acoustic impedances). For the well acoustic impedance the compressional sonic and bulk density logs are used. For the well elastic impedance inversion, an elastic impedance log at each well is computed along the lines of Connolly (1999). The same inversion procedure is followed for elastic impedance, with the exception that a target elastic impedance log is used to construct the well impedance model. Three sets of elastic impedance volumes were generated: 24 to 32 degrees (center angle of 28 degrees); 32 to 40 degrees (center angle of 36 degrees); and 40 to 48 degrees (center angle of 44 degrees). The well elastic impedance was computed at each center angle. One acoustic impedance volume using a restricted near angle aperture of zero to 12 degrees was computed.

Lambda-mu-rho (LMR) attributes: To compute these attributes, the compressional (Rp) and shear (Rs) zero-offset reflectivity series are extracted from the CMP data using the methodology put forth by Fatti et al. (1994). The compressional and shear reflectivities are then inverted to obtain the acoustic and shear acoustic impedances using the aforementioned constrained GLI inversion techniques. Compressional acoustic impedance logs and the initial model are constructed with the bulk density and compressional sonic logs, and shear impedance logs (and initial model) are constructed using the bulk density and shear sonic logs. For wells without shear wave data, a localized mudrock line for wet sands and shales can be computed, and gas sands estimated using Biot-Gassmann-Gertsma type equations. Using the computed impedance volumes, lambda-rho (LR) and mu-rho (MR) can be calculated as described by Goodway, et al. (1997). LR is proportional to the incompressibility and MR is proportional to rigidity. Three sets of lambda-rho and mu-rho were generated with maximum incident angles of 32, 40 and 48 degrees.

Methodology: As demonstrated by Castagna (1993, 2001), Verm and Hilterman (1995), Ross (2000), Ross and Sparlin (2000) and others, two-attribute crossplot analysis is a robust approach to anomaly determination. This study uses attribute crossplotting of the base attributes from each method as opposed to estimating the best compound AVO attribute (combinations of both attributes to make new attributes. i.e. A*B, lambda/mu, etc…) To this end, crossplots of A and B, AI and EI, LR and MR are examined for each angular aperture. The crossplot data is for a narrow temporal window (approximately 40 ms) extracted between two reflectors bracketing the known reservoir. Background or host rock trends and anomalous pairs of data are identified and

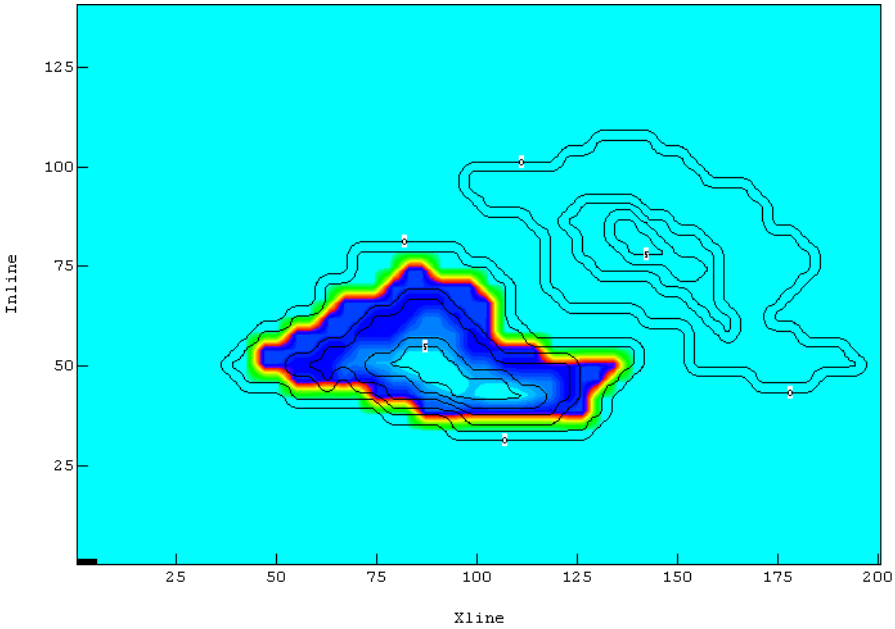

Figure 1: Intercept-gradient (A-B) crossplot anomaly with 1 ms sand isochrons. Gas-sand is towards the southwest, wet sand towards the northeast.

mapped back to the seismic volume. An interval horizon slice through the crossplot volume is extracted using the envelope amplitude. The gas sand anomaly is then compared to assess the apparent extent of the known reservoir for each AVO methodology.

Analysis of large aperture results

Interval data slices from the A-B, AI-EI, and LR-MR crossplot analysis using the large angle apertures are shown in Figures 1 through 3, respectively. Overlaying each color anomaly map is the isochron of the reservoir sand thickness in two-way time (ms). The gas sand lobe is towards the southwest, the wet sand towards the northeast. For each methodology, all of the attributes detect the thickest section of the gas-charged sand lobe. However, the traditional A-B slice extends over a larger portion of the known anomaly (Figure 1) than the others, extending out towards the zero isochron contour line. Considering the A-B application does not require any additional post stack inversions, this approach (when CMP data is available) is straightforward.

Discussion

There are several discussion points to address in comparison of these AVO applications. First, in this comparison I am showing differences in area and not volume. Since all of the techniques illustrate the thickest portion of the gas sand, the differences between them may be exaggerated by areal comparison. Also, one might argue that typical seismic noise and resolution issues might make it very difficult to see the thinner reservoir as observed with the A-B display, and that by areal comparisons all three techniques are essentially the same.

It is also important to consider the contributions of wells. Both the LMR and EI approaches require post stack inversions that are constructed with an initial model. Since the initial model most often requires well log input for accuracy, lack of, or a dearth of well control points might cause an inferior initial model, and subsequently a poor inversion result. Similar arguments about poor initial models can also be levied against the shear impedance model where shear wave logs are not always available.

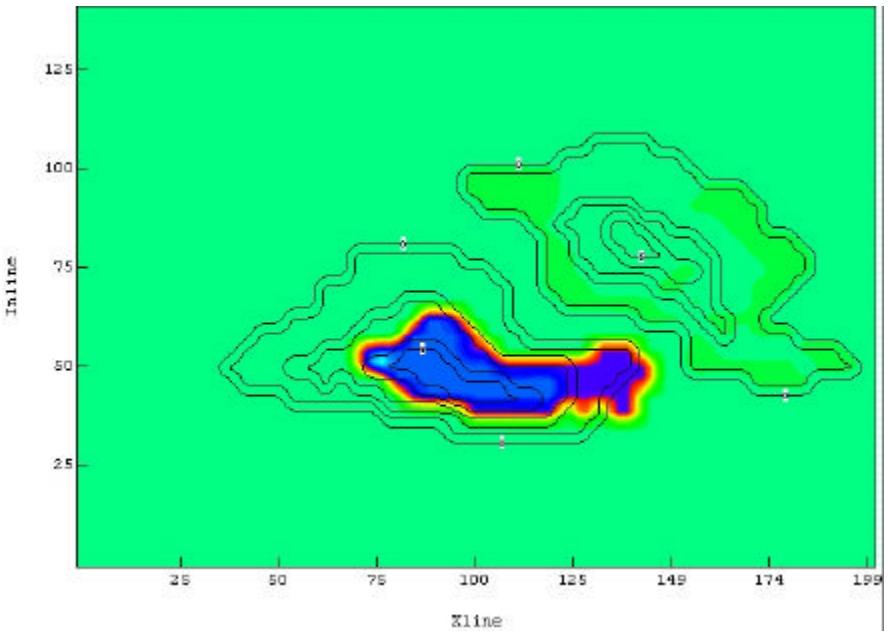

Figure 2: Acoustic impedance – elastic impedance (AI-EI) crossplot anomaly with 1 ms sand isochrons. Gas-sand is towards the southwest, wet sand towards the northeast.

Finally, there are seismic section interpretation issues that enter into the selection process of which attribute is "best." While in these figures the A-B areal extent is larger than the inversion attributes, the inversion anomalies from LMR and EI are temporally sharper (higher frequency, higher resolution) than the A-B anomaly. Since the A-B method makes no attempt to remove the wavelet, the A-B anomaly appears ungainly when compared to the inversion seismic displays. However, it appears that by not attempting to remove the wavelet, a larger areal response is obtained.

Conclusions

For each field and reservoir, a reservoir manager needs to be aware that not all AVO attributes selected will give the same results, and some may be more robust than others. Modeling and comparing all AVO attributes available in a similar manner should prove useful in selecting the best AVO input for reservoir modeling and simulation. For this model, geology and reservoir, based on areal extent, the traditional A-B attribute with the large aperture recovers more of the known field than the EI and LMR techniques. The EI and LMR inversion-based results appear similar in terms of areal extent and have better temporal resolution than the A-B gas sand anomaly.

References

Castagna, J. P., 1993, Petrophysical imaging using AVO: TLE, 12/3, 172-178.

Castagna, J.P., 2001, Recent advances in seismic lithologic analysis: Geophysics, 66, 42-46.

Connolly, P., 1999, Elastic impedance: TLE, 18/4, 438-452

Fatti, J.L., Smith, G. C., Vail, P.J., Straus, P. J., and Levitt, P. R., 1994, Detection of gas in sandstone reservoirs using AVO analysis: A 3-D seismic case history using the Geostack technique: Geophysics, 59, 1362-1376.

Goodway, W., Chen, T., and Downton, J., 1997, Improved AVO fluid detection and lithology discrimination using Lame petrophysical parameters: "Lambda-Rho", "Mu-Rho", Lambda/Mu fluid stack", from P and S inversions: 67th Ann. Internat. Mtg., Soc. Expl. Geophys., Expanded Abstract, I, 183-186.

Ross, C. P., 2000, Effective AVO crossplot modeling: A tutorial: Geophysics, 65, 700-711.

Ross, C. P., and Sparlin, M.A., 2000 Improved crossplot analysis using visualization techniques: TLE, 19/11, 1188-1199.

Verm and Hilterman, 1995, Lithology color-coded seismic sections: The calibration of AVO crossplotting to rock properties: TLE, 14/8, 847-853.

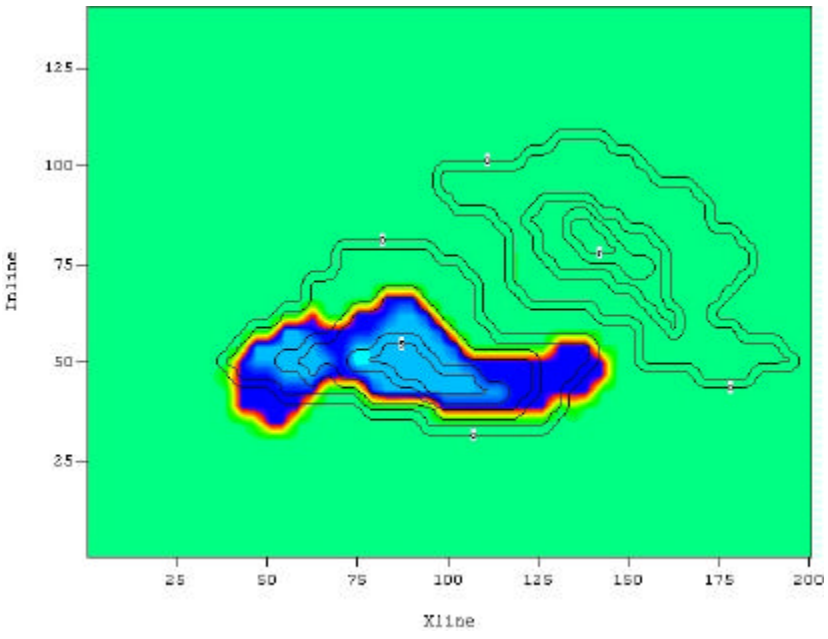

Figure 3: Lambda-rho – Mu-rho (LR-MR) crossplot anomaly with 1 ms sand isochrons. Gas-sand is towards the southwest, wet sand towards the northeast.

Reflection Impedance

Lúcio T. Santos, Martin Tygel, IMECC/UNICAMP, and Antonio C. Buginga Ramos, PETROBRAS S/A, Brazil

Abstract

AVO is now an established technology and has been widely deployed as a lithology indicator and also as a direct hydrocarbon indicator. In recent years this technology has become a routine processing and its application to large 3D volumes has relied on the use of near- and far-offset stack volumes. These volumes greatly reduce the amount of pre-stack information that needs to be stored for standard AVO processing. Additionally, these volumes are easily converted into usual AVO attributes, like intercept and gradient, which can then be interpreted in terms of anomalies and calibrated with well logs. Reservoir characterization studies make use not only of these traditional AVO attributes but also impedance volumes. The near-offset, or the intercept, stack volume offers a natural way of obtaining acoustic impedance volume through the use of post-stack inversion algorithms. However, to invert far-stack volume one needs an approach capable of estimating impedances for a variable incidence angle. This approach has been described in the elastic impedance function presented by Connolly (1999). In this work we propose an approach called reflection impedance, which is based on constant ray parameter and a power relationship between density and S-wave velocity. This new method proved to be of better accuracy for angular impedance estimation and reflection coefficient recovery when compared with the elastic impedance approach.

Introduction

In recent years there has been an enormous increase in the amount of 3D seismic data processed with AVO purpose. The most economical form of processing large volumes of seismic data to obtain AVO attributes involves obtaining near- and far-offset stacks. These stacks have been intensively used not only to obtain traditional AVO attributes, like intercept and gradient, but also as input of post-stack inversion algorithms to yield acoustic impedance (AI) volumes that help in reservoir characterization. The near-offset stack can be tied to synthetics obtained from acoustic impedance changes derived from well logs. After calibration, the near-offset stacks can then be inverted back to acoustic impedances using off-the-shelf post-stack inversion algorithms, which use the well log impedances as constraints. The missing part of this process was how to invert the far-offset stacks? The answer to the question came from the elastic impedance (EI) approach presented by Connolly (1999), which generalizes the acoustic impedance concept for variable incidence angle. In other words, the EI provides a way to calibrate and invert nonzero-offset seismic data just as AI does for zero-offset data.

One advantage of the EI method is that it correlates directly to rock properties, like α/β ratio (P- to S-wave velocity ratio), instead of being an attribute that relates to contrasts of elastic properties of neighboring rocks (like most AVO attributes).

In this work we demonstrate a new approach to obtain nonzero-offset impedance estimates to be used as calibration for nonzero-offset seismic data. We called this approach reflection impedance (RI). Basically, RI is based on constant ray parameter as opposed to constant incidence angles, as proposed by Connolly (1999). Also, the new approach assumes a power relation between density and S-wave velocity while the EI approach assumes a constant $K=(\beta/\alpha)^2$. As a result, the new approach greatly improves the accuracy of the impedance estimates, which can be critical in case of subtle amplitude anomalies.

Normal Incidence: Acoustic and Elastic

For a given normal reflected ray, parameterized by the traveltime τ, the normal P-P reflection coefficient is given by

$$R(\tau,\Delta\tau)=\frac{Z(\tau+\Delta\tau)-Z(\tau)}{Z(\tau+\Delta\tau)+Z(\tau)} \qquad (1)$$

where

$$Z(\tau)=\rho(\tau)\,\alpha(\tau) \qquad (2)$$

is the acoustic impedance function, $\rho(\tau)$ is the density function, $\alpha(\tau)$ is the P-wave velocity function, and $\Delta\tau$ is the traveltime increment, chosen to be sufficiently small. Observe that we also consider that the elastic parameters are being parameterized by the traveltime. We will also consider the P-P reflectivity function,

$$r(\tau)=\lim_{\Delta\tau\to 0}\frac{R(\tau,\Delta\tau)}{\Delta\tau}=\frac{1}{2}\frac{Z'(\tau)}{Z(\tau)}, \qquad (3)$$

where the prime denotes derivative with respect to τ.

Non-Normal Incidence: Acoustic

For a general reflection, not necessarily normal, the acoustic reflection coefficient is given by

$$R_a(\tau,\Delta\tau) = \frac{I(\tau+\Delta\tau) - I(\tau)}{I(\tau+\Delta\tau) + I(\tau)}, \quad (4)$$

where

$$I(\tau) = \rho(\tau)\ \alpha(\tau)\ \sec\theta(\tau) \quad (5)$$

where $\alpha(\tau)$ denotes the acoustic velocity, may be called acoustic reflection impedance function, $\theta(\tau)$ is the incidence angle and, as before, $\rho(\tau)$ is the density. The quantity I(τ) will be called acoustic reflection impedance.

Elastic Impedance

Connoly (1999) starts the derivation of the EI (elastic impedance) function by setting the linearized approximation of P-P reflection coefficient given in Aki and Richards (1980) equal to one half of logaritmitic change in EI:

$$\tilde{R}_{pp}(\theta) \approx \frac{1}{2}\Delta\ln(EI), \quad (6)$$

where the tilde indicates the use of an approximation for R_{pp}. Upon integration and exponentiation on both sides of this equation, and setting the integration constant to zero, one obtains:

$$EI = \rho^{(1-4K\sin^2\theta)}\ \alpha^{(\sec^2\theta)}\ \beta^{(-8K\sin^2\theta)}, \quad (7)$$

where β represents the S-wave velocity.

Reflection Impedance

The concept of reflection impedance, as introduced in Moraes (2000), is in essence similar to the EI function presented above, however, the ray parameter, instead of the incidence angle, is considered constant. After algebraic manipulations in the exact P-P reflection coefficient formula and the assumption that there is an exponential dependency between density and S-wave velocity ($\rho = b\,\beta^{\gamma}$, with b and γ as empirical constants to be determined), we obtain the following expression for reflection impedance:

$$RI = \rho\ \alpha\ \sec\theta\ \exp\left[-2(2+\gamma)\left(\frac{\beta}{\alpha}\right)^2\ \sin^2\theta\right] \quad (8)$$

Discussion

In order to compare the accuracy of EI and RI functions presented above we use the approximation of P-P elastic reflection at a point between two media with local parameters given by ρ_i, α_i, β_i, with i representing the layer index in each side of the interface, such that:

$$R_{PP}^{EI} \cong \frac{EI_2 - EI_1}{EI_2 + EI_1}, \quad \text{and} \quad (9)$$

$$R_{PP}^{RI} \cong \frac{RI_2 - RI_1}{RI_2 + RI_1}. \quad (10)$$

Here, to compute RI we used the following formula for γ:

$$\gamma = \frac{\ln(\rho_2/\rho_1)}{\ln(\beta_2/\beta_1)}. \quad (11)$$

We used equations (9) and (10) to compare the reflection coefficients responses computed with both methods. The model used in the computations is shown in Table 1 and the results are shown in Figure 1. The response computed based on the elastic impedance method deviates not only from the exact Zoeppritz formula for reflection coefficients but also from the linearized approximation for R_{pp}. The response computed from the reflection impedance method (11), agrees with the exact Zoeppritz formula for R_{pp}. Therefore there is a significant gain in accuracy provided by the reflection impedance method compared to the elastic impedance method.

Layer	Rock	α (km/s)	β (km/s)	ρ (g/cm^3)
1	shale	3.27	1.65	2.20
2	sandstone	3.04	1.74	2.05
3	shale	3.27	1.65	2.20

Table 1 – Elastic properties used to model EI and RI curves

Figure 2 shows the comparison of a normalized AI curve (EI(0)) with a normalized 30^0 EI curve for an oil sand reservoir encased in marine shales. Figure 3 used the same well log data and the normalized AI curve compared with a 30^0 RI curve. Figure 4 compares the normalized responses of both elastic and reflection impedance methods for the 30^0 incidence angle case. The normalized EI and RI curves are very similar outside the reservoir zone, but disagree in the reservoir zone, possibly because the RI method senses more the changes in α/β ratio. Therefore, the observed differences are in part related to the higher degree of accuracy obtained by the RI

method compared to the EI method. The apparent improved discrimination of the reservoir zone in the RI curve can be a key for the use of this method instead of the EI.

Conclusions

The RI method proved that it recovers back the exact reflection coefficient curve from a simple form of approximation. Additionally, when used to produce angle dependent impedances, the proposed RI method showed greater accuracy and improved degree of discrimination compared to the EI method.

References

Connolly, P., 1999, Elastic Impedance: The Leading Edge, v. 18, p. 448-452.

Moraes, J. A. C, 2000, Construction of reflection impedance sections by means of migration to zero offset. M.Sc. Disert., Fac. of Mech. Engineering, State University of Campinas (FEM/UNICAMP) (in Portuguese).

Acknowledgments

We would like to thank PETROBRAS for permission to publish this work.

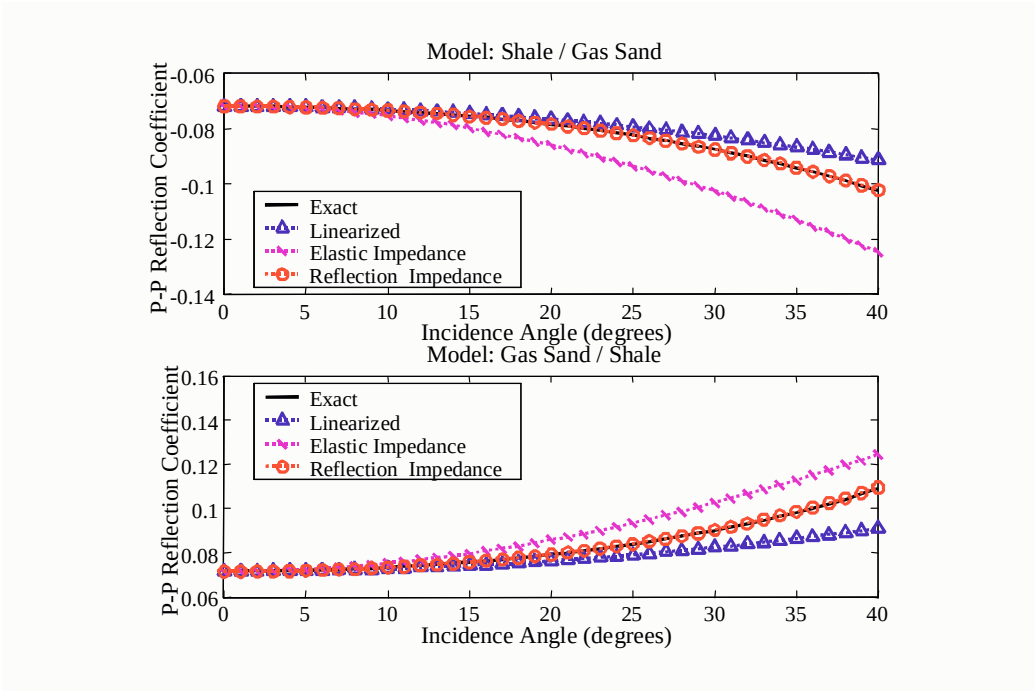

Figure 1- Non-normal P-wave reflectivity responses (R_{pp}) for the model presented in table 1. Notice the better agreement between R_{pp} computed from the reflection impedance and the exact Zoeppritz formula. The response computed from elastic impedance deviates from the exact and the linearized approximation for R_{pp}.

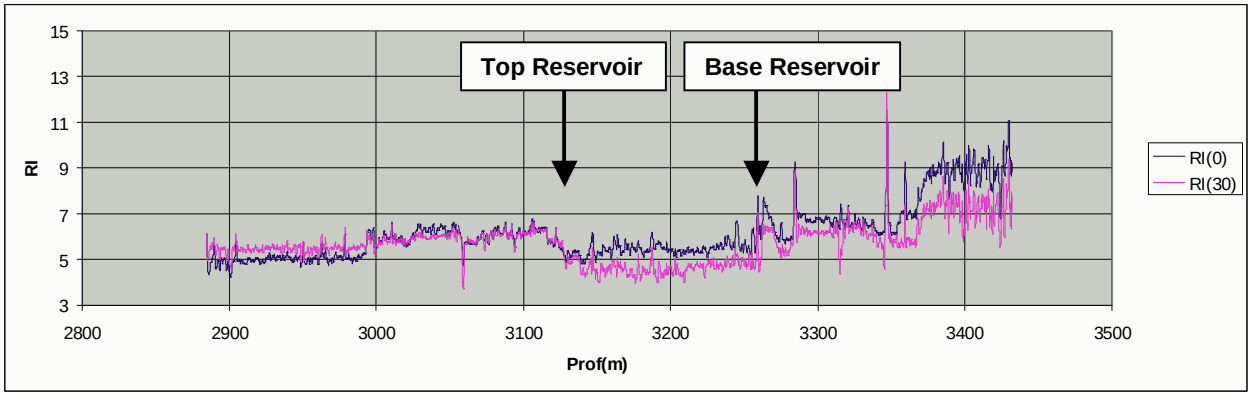

Figure 2 – Comparison of a normalized AI curve (EI(0)) with a normalized 30^0 EI curve for an oil sand reservoir encased in marine shales.

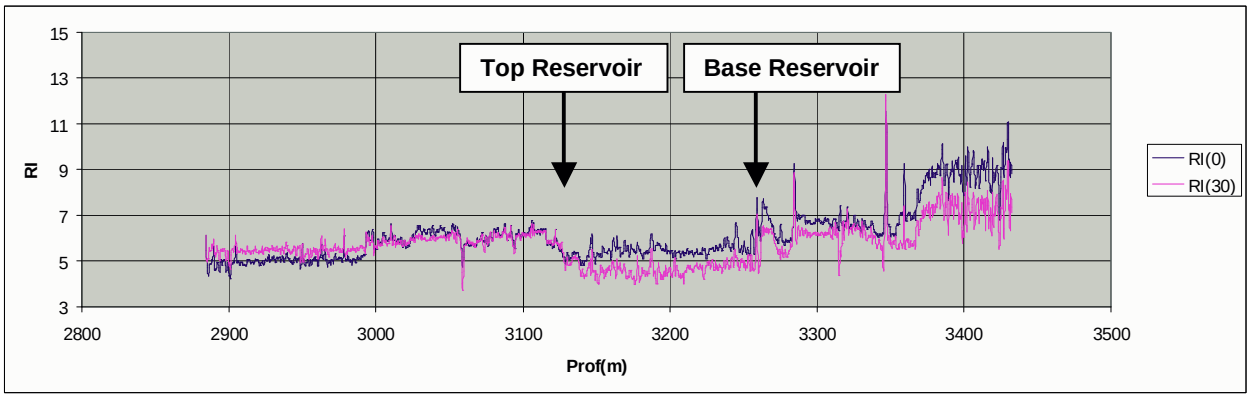

Figure 3 – Comparison of a normalized AI curve (RI(0)) with a normalized 30^0 RI curve for an oil sand reservoir encased in marine shales.

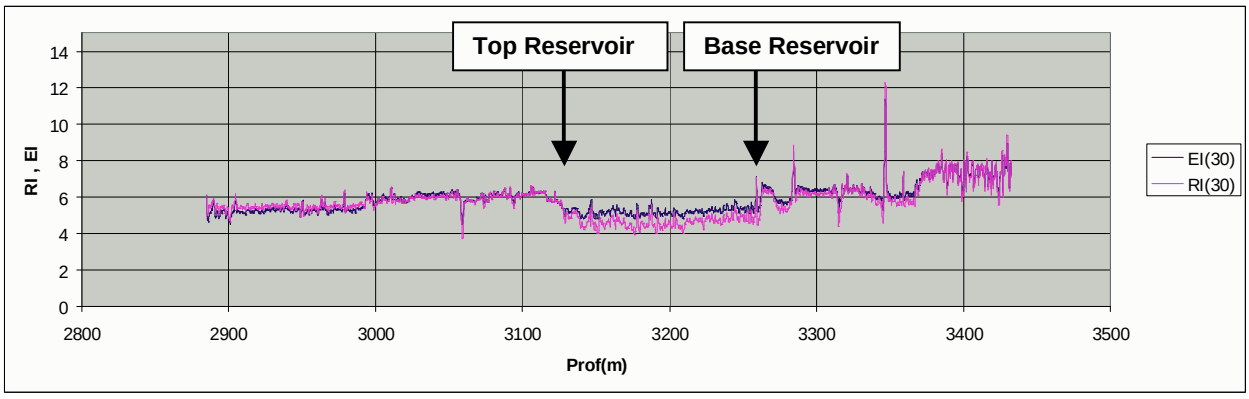

Figure 4 – Comparison of a normalized AI curve (RI(0)) with a normalized 30^0 RI curve for an oil sand reservoir encased in marine shales.

Shear Waves AVO Azimuthal Analysis in Vacuum Field, New Mexico

Luis Henrique Amaral, Petrobras S/A, Brazil

Abstract

Shear wave amplitude versus offset (AVO) analysis was used in Phase VII Reservoir Characterization Project in Vacuum Field, New Mexico, for porosity and permeability estimation and time-lapse investigation of the Upper San Andres reservoir.

DeVault (1998) pointed out that plane-wave reflection coefficients for shear waves can be inverted for density contrast, fracture density contrast and shear velocity contrast.

The interpretation of the AVO attributes can help to estimate the porosity and permeability of the reservoir. The result obtained for porosity agrees with the data from well logs, especially in the center of the reservoir area, around the producers and injector wells. Upper San Andres reservoir is a dolomite where most of the permeability is provided by vertical fractures. The fracture density was particularly efficient in portraying the intense fracturing between CVU-97 and CVU-200, confirmed by the oil production increase after CO2 injection.

The time-lapse analysis showed variation in the density between the pre and the post CO2 injection in the northern part of the reservoir, with agreement with the production wells in this area.

AVO attributes inversion proved to be a reliable method for reservoir attribute determination and time-lapse analysis, and provides an important link between seismic data and rock properties.

Introduction

Reservoir characterization is a multidisciplinary study which aims at a more economic and efficient exploitation of oil fields. Vacuum Field, the object of this research, is a Permian dolomitic reservoir, located in the Permian Basin of west Texas(figure 1).

Several studies have been conducted in Vacuum Field by the Reservoir Characterization Project. The objective of Phase VII was to ascertain the porosity, permeability, fluid and flow characterization of the San Andres reservoir. Production of hydrocarbons generates changes in the physical properties of the reservoir over time. Time-lapse analysis dynamically characterizes the reservoir, and can help to evaluate and predict reservoir performance.

Figure 1. Location of Vacuum Field, New Mexico

Porosity results were consistent with the well-log derived porosity. Estimates of fracturing were interpreted here as a measurement for permeability. This confirmed the intense fracturing expected in the CVU-97 and CVU-200 area, and indicated at the northwest corner of the reservoir the absence of fracturing. Time-lapse analysis was consistent with fluid production data.

Azimuthal AVO

San Andres reservoir can be approximated to an isotropic matrix with a set of vertical fractures oriented at 122 degrees from north. The model which best fits to San Andres characteristics is the horizontal transverse isotropy, or HTI.

A HTI medium can be defined as a “first-order” model for azimuthal anisotropy with a horizontal axis of symmetry. Figure 2 shows modelling results for reflection coefficients of an interface between an isotropic medium and a HTI medium for P waves. The reflection coefficients are affected by the azimuth.

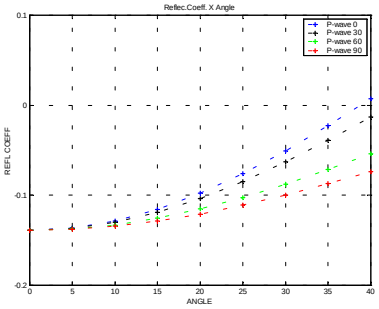

Figure 2. Reflection coefficient variation according to incidence angle and azimuth, for P waves in a HTI medium. 0 means azimuth parallel to the isotropy plane and 90 azimuth parallel to the symmetry plane

Ruger (1996) derived the solutions for the reflection coefficients of shear waves in a HTI medium, as a function of azimuth and incidence angle:

$$R_{S_1}^{str}(\theta) = -\frac{1}{2}\left(\frac{\Delta V_s}{V_s} + \frac{\Delta\rho}{\rho}\right) + \left(\frac{7}{2}\frac{\Delta V_s}{V_s} + 2\frac{\Delta\rho}{\rho}\right)\sin^2\theta$$

$$R_{S_1}^{sym}(\theta) = -\frac{1}{2}\left(\frac{\Delta V_s}{V_s} + \frac{\Delta\rho}{\rho}\right) + \frac{1}{2}\left(\frac{\Delta V_s}{V_s} - \Delta\gamma\right)\tan^2\theta$$

$$R_{S_2}^{str}(\theta) = -\frac{1}{2}\left(\frac{\Delta V_s}{V_s} + \frac{\Delta\rho}{\rho} - \Delta\gamma\right) + \frac{1}{2}\left(\frac{\Delta V_s}{V_s} - \Delta\gamma\right)\tan^2\theta$$

$$R_{S_2}^{sym}(\theta) = -\frac{1}{2}\left(\frac{\Delta V_s}{V_s} + \frac{\Delta\rho}{\rho} - \Delta\gamma\right) + \left[\frac{7}{2}\left(\frac{\Delta V_s}{V_s} - \Delta\gamma\right) + \frac{2\Delta\rho}{\rho} + \frac{1}{2}\left(\frac{V_p}{V_s}\right)^2\left(\Delta\varepsilon^v - \Delta\delta^v\right)\right]\sin^2\theta$$

Vp, Vs and ρ are the average values between the two media. ε^V, δ^V and γ are anisotropy parameters.

The AVO azimuthal analysis will be performed in the symmetry plane and in the isotropy plane. The waves polarized within the isotropy plane are called S1 or fast shear waves while the waves polarized in the plane formed by the slowness vector and the symmetry-axis are called S2 or slow shear waves.

The equations for S waves azimuthal AVO can be expressed in terms of intercepts (A) and gradients (B):

$$R = A + B\sin^2\theta$$

The system of equations for shear waves can be expressed in matrix form:

$$\begin{bmatrix} A_{S_2}^{str} \\ B_{S_2}^{str} \\ A_{S_1}^{str} \\ B_{S_1}^{str} \\ A_{S_1}^{sym} \\ B_{S_1}^{sym} \end{bmatrix} = \begin{bmatrix} -\frac{1}{2} & -\frac{1}{2} & \frac{1}{2} \\ \frac{1}{2} & 0 & -\frac{1}{2} \\ -\frac{1}{2} & -\frac{1}{2} & 0 \\ \frac{7}{2} & 2 & 0 \\ -\frac{1}{2} & -\frac{1}{2} & 0 \\ \frac{1}{2} & 0 & -\frac{1}{2} \end{bmatrix} \begin{bmatrix} \frac{\Delta V_S}{V_S} \\ \frac{\Delta\rho}{\rho} \\ \Delta\gamma \end{bmatrix}$$

There are 3 unknowns, $\frac{\Delta V_S}{V_S}$, $\frac{\Delta\rho}{\rho}$ and $\Delta\rho$, and 6 equations, which defines an overdetermined system. The use of shear waves for the solution of velocity, density and shear wave splitting parameters avoids reliance in empirical constraints, like Vp/Vs relationships. The system can be solved for shear velocity, density and shear wave splitting parameter variation across the interface

Porosity and Permeability Estimation

Figure 3 shows a map of porosity based on well data compared to a map of the density contrast between San Andres and Grayburg. The density contrast will be interpreted as an expression of the porosity in the Upper San Andres. Some assumptions have been made to achieve these results. First, the density contrast has the same behavior of the San Andres porosity. When it is correlated to porosity, it is implicit that the density of Grayburg is constant over the entire reservoir. However, for variations in San Andres density to be linearly related to porosity, implies that there are no variations in the matrix mineralogy. How much the results are affected by deviations from these assumptions must be taken into account when interpreting the density contrast map. The density contrast map detects a higher trend of porosity in the east-southeast area and overestimates the difference between the center-northeast trend and the center-west trend. There are some possible reasons for the differences between these two maps.

A)

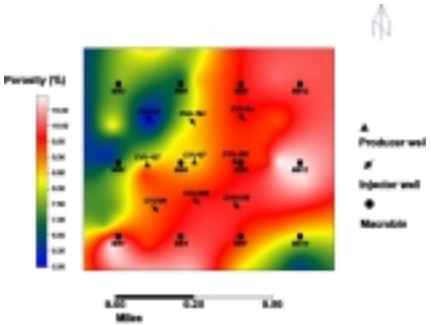

B)

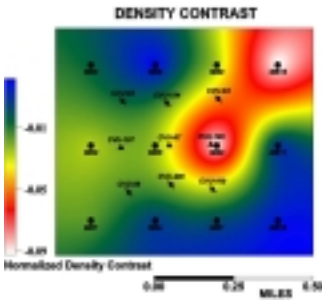

Figure 3. A) Porosity map from Upper San Andres, based on well data B) Map of density contrast from Upper San Andres.

Figure 4 shows the well log derived porosity contrast map between Grayburg and Upper San Andres. The porosity of Grayburg is not homogeneous and its variations affect the density contrast map. In the southern area the porosity contrast is very low, which may explain the low density contrast.

The San Andres reservoir is composed basically of a dolomite matrix. However, anhydrite is abundant as a pore-filling cement and as replacement for dolomite. There is a high concentration on the southeast part of our reservoir area in the Upper San Andres, while the Grayburg is free of dolomite. It suggests a decrease in density contrasts between the San Andres and the Grayburg, as seen in the density contrast map.

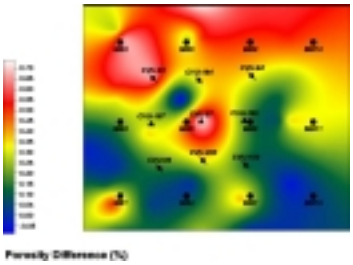

Figure 4. Porosity contrast between Grayburg and Upper San Andres.

The delineation of areas with higher permeability can be achieved by fracture density estimation. The splitting parameter γ, which is a measurement of shear wave anisotropy, is linearly related to fracture density, so the variations in γ will be an expression of variations in reservoir fracturing.

Figure 5 is a map of the splitting parameter contrast between the base of the Grayburg and Upper San Andres. Fracturing increases downward, being very small in Grayburg and increasing within the Lower San Andres. The fracture contrast should represent mainly the fractures in the Upper San Andres. The fracturing is more intense in the center of the field, especially around well producer CVU-97. There is also a well defined trend northeast-southwest. The negative values in the northwest and southeast corners indicate a more intense fracturing in the Grayburg.

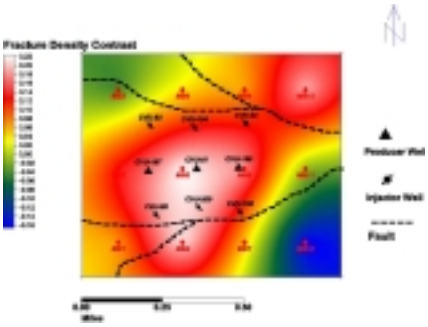

Figure 5. Fracture density contrast map of Upper San Andres. Negative values mean that Grayburg is more fractured than San Andres.

The northwest area of the reservoir has been interpreted as affected by porosity generated by matrix dissolution and dolomite substitution, and random distribution within the matrix, without any dominant orientation. The rock behavior, related to seismic waves, would be closer to an isotropic model, rather than a HTI one. The fracture density map would indicate a very low $\Delta\gamma$.

Around the injector and producer wells there is a fair agreement between the fracture density map, observed production and CO2 injection results. CVU-97 had the highest increase in oil production in the field, resulted from CO2 injection, which confirms the presence of intense fracturing around the well (figure 7).

Time Lapse Analysis

AVO was inverted for fracture density and density estimation, , in the pre and post CO2 injection datasets separately. The objective was to investigate observable changes introduced by the CO2 injection in the reservoir.

Shear velocity and fracture density contrasts did not present any noticeable changes. Density, however, experienced a drop in the northern portion of the time-lapse area, expressed in figure 6. Figure 7 shows the production of CVU-97. This well had the best response for the CO2 injection in the time-lapse area. Well CVU-104 (figure 8), south of injector CVU-200, had no changes in production, which indicates a mobilization of the oil towards north.

The production of wells closer to injectors CVU-93, CVU-194 and CVU-94 remained stable. Under their area of influence, only CVU-97 and a small breakout in CVU-196 showed the effects of CO2 injection.

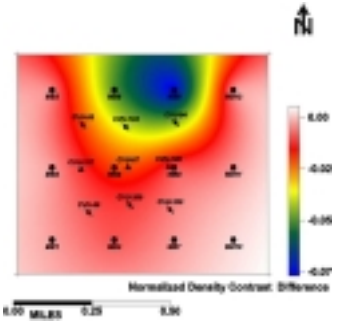

Figure 6. Density contrast difference, between pre and post CO2 injection data.

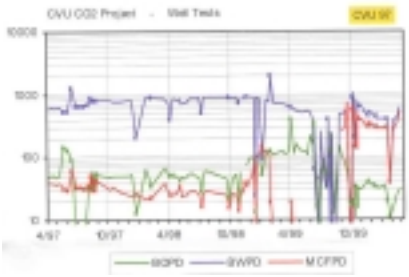

Figure 7. CVU-97 production.

Figure 8. CVU-104 production

Well CVU-87, which is located in the northern portion of the survey, however, showed an increase in gas production (figure 9). It suggests that the displacement of the gas injected was in the northern direction, and that the CO2 did not mix entirely with the oil, but remained as a gas and concentrated in this area, causing a drop in density.

In CVU-97 the changes in density were not so evident because most of the CO2 mixed with the oil, remaining as a liquid, with higher density than as a gas.

Figure 9. Production of CVU-87.

Conclusions

The results obtained for density contrast proved the method to be robust. The map of density contrast offered a straightforward correlation to the porosity map, especially in the areas with high fold.

The fracture density map also offered, in the center of the survey, a response consistent with well production and CO2 injection results. The highest fracture density was detected between CVU-200 and CVU-97, where the oil production increase caused by CO2 injection was also concentrated.

Although the results obtained were consistent with most information available from other sources, like well productivity, shear wave anisotropy analysis, CO2 injection and well porosity, geology must be taken into account when interpreting the results. The use of constraints is necessary, and the quality of the parameters interpretation is in direct dependence on the knowledge of the reservoir's geology.

The time-lapse analysis showed a variation in density contrast, especially in the northern area and around CVU-97, and suggests a fluid flow towards north. These results are corroborated by well production data.

AVO analysis of shear waves improves the characterization of a reservoir, and can provide a link between seismic data and rock properties.

References

Amaral, L.H., 2001, Shear waves azimuthal AVO analysis, Vacuum Field, New Mexico, Ms Thesis, Colorado School of Mines, T-5467, 107 p.

DeVault, B., 1998, 3D seismic pre-stack multicomponent amplitude analysis, Vacuum Field, Lea County, New Mexico, PhD Thesis, Colorado School of Mines, T-5076 , 192 p.

Ruger, A., 1996, Reflection coefficients and azimuthal AVO analysis in anisotropic media, PhD Thesis, Colorado School of Mines, T-4946, 170 p.

Acknowledgements

I wish to thank Petrobras for the financial support and Tom Davis, for the opportunity to work with Reservoir Characterization Project.

The generation of a rock and fluid properties volume via the integration of multiple seismic attributes and log data.

Matthew Carr, Richard Cooper, Maggie Smith, M. Turhan Taner, Gareth Taylor – Rock Solid Images, Houston, Texas, USA*

Abstract

We present a systematic seismic reservoir characterization workflow that integrates log and seismic data using an artificial neural network.

Seismic attributes are examined both qualitatively and quantitatively to determine the best discriminators of rock and fluid properties. These attributes are systematically classified using an artificial neural network, the Kohonen self-organizing map (K-SOM) algorithm. Ultimately the classified litho-facies volume is calibrated to available well control by applying the K-SOM technology to well-derived data.

The product is a seismic-scale rock and fluid properties reservoir model that is consistent with borehole and surface seismic data.

The workflow is applied to the characterization of a Vicksburg-age reservoir in South Texas.

Introduction

Seismic attributes have been used for many years as a way of qualitatively inferring rock and fluid properties from seismic data. These approaches have, in general, involved the time-consuming and laborious examination of numerous attributes in an attempt to identify elusive or misleading signatures that may be indicative of the presence of hydrocarbons, e.g. a low frequency shadow beneath the reservoir, a polarity or phase reversal at the reservoir periphery and numerous impedance and amplitude-related direct hydrocarbon indicator (DHI) effects. More recently, this process has been automated by employing a variety of artificial neural network-based classifiers. Some of these methods also use borehole data to further constrain and calibrate this classification.

For example, Russell *et al*, (1997) describe a method for seismic analysis which makes use of artificial neural networks (ANN) to predict log-curves from multiple sets of seismic attributes. An alternative method was presented by Walls *et al*, (1999) for training a neural network using model-driven seismic attributes. This trained network is then applied to surface seismic for lithology classification. Morice *et al*, (1996) describe a method for using Kohonen self- organizing maps for facies analysis from seismic data.

Kohonen self-organizing maps (K-SOM) can be effective tools for defining seismic classes or facies. However, compared to other ANN based methods, it has proven difficult to calibrate the resulting classification with borehole data.

This paper presents a new method for employing borehole data to calibrate a K-SOM data-set. The method itself is described, and a result is given for a Vicksburg-age reservoir in South Texas.

Attribute Calculation, Calibration and Classification

The generic workflow employed in this study involved the computation, classification and calibration of seismic attribute data. The primary elements of this workflow are depicted in Figure 1.

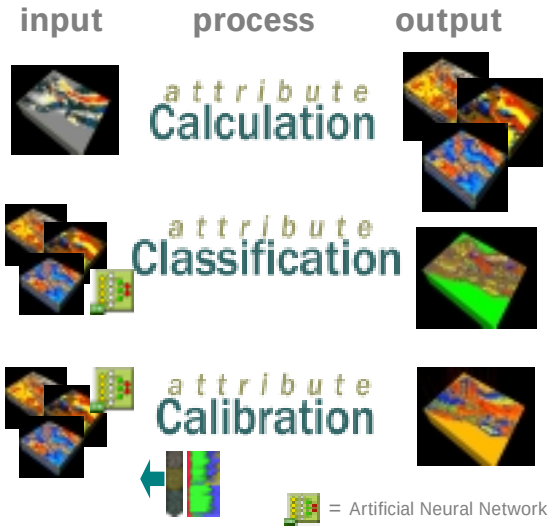

Figure 1. Workflow

Attribute Calculation

It is possible to compute two broad classes of seismic attributes - Physical Attributes and Geometric Attributes. In general, physical attributes respond to variations in physical properties and include Hilbert transform-derived attributes, AVO-related attributes and impedance attributes. These attributes may be computed either sample-by-sample (instantaneous physical attributes) or at the peak of the envelope (wavelet physical attributes). Geometric attributes, which respond to variations in reservoir morphology, e.g. structure and stratigraphy, are a manifestation of the spatial and temporal variation of physical attributes since they are computed over a user-defined time and space gate. Attributes such coherence, semblance, similarity and other attributes designed to extract morphological elements from seismic data fall within this class.

In this workflow, a suite of physical and geometric attributes is computed and visually examined to determine whether "classic" DHI's are present and to better image fault geometries and fluvio-deltaic morphologies. Contemporary voxel-based visualization tools allow for the rapid reconnaissance of numerous attributes thereby enhancing the interpreter's ability to conceptualize a broad spectrum of possible reservoir morphologies.

By coupling a statistical technique, such as principal component's analysis, to the visualization process, we are able to determine which attributes carry the most important diagnostic weight.

Those attributes that offer the best discrimination are then classified by the K-SOM tool.

Attribute Classification and Calibration via Kohonen Self Organizing Maps (K-SOM)

Though the classification of n-dimensional attribute data is complex in detail, the method is simple in concept.

We make two key assumptions within our workflow:

1. Borehole log-curves are analogous to seismic attributes. (Each is a representation of a sub-surface property. Borehole log-curves are formation attributes defined by the tool in use. Seismic attributes are mathematical representations of the sub-surface defined by the algorithm in use.)

2. Assuming the log and seismic data are appropriately preconditioned and of sufficient quality, we would expect both to be systematically but separately related to lithofacies.

The Kohonen algorithm is employed twice; once to classify the seismic attribute data, and once to classify the borehole information. The K-SOM method separates the well log data (density, neutron, sonic, gamma, resistivity) into 100 classes with similar log response, which implies similar petrofacies. It also separates the seismic attributes into 100 classes of similar seismic response, which implies similar lithofacies.

We make extensive use of "pseudo-wells" within the log-based classification step. Pseudo-wells represent additional log-based models of the reservoir, derived via rock-physics modeling, to simulate ranges of reservoir properties expected within the reservoir, but not necessarily encountered in available borehole information.

Core and log analysis is performed to determine the relationship between the log-derived Kohonen classes and reservoir properties. During this process, we sub-set the initial 100 classes into a reduced set of 12 "lithofacies".

The same grouping criteria is then imposed on the time to depth derived seismic classes at each well. Hence we obtain a relationship between our original reservoir classes and the seismic classes. This relationship is then used to map physical properties to the seismic-derived Kohonen classes.

Case Study

An example is given for a Vicksburg-age reservoir in South Texas.

The seismic survey covered approximately 50 square miles with 4 wells available for analysis, two of which encountered oil and saturated pay sands. The fluvio-deltaic system is located at a depth of approximately 4,200 feet and is shown in Figure 2.

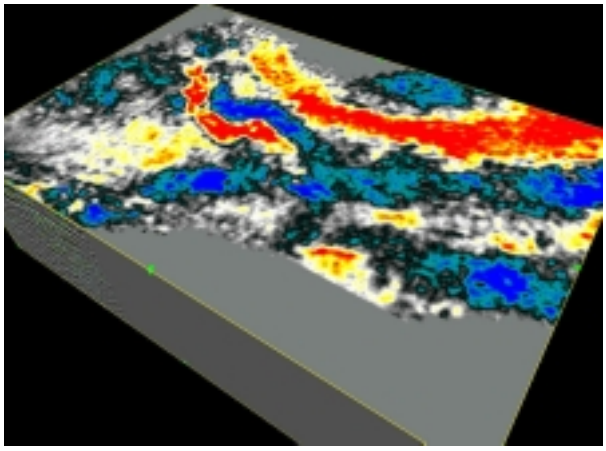

Figure 2 . Input amplitude volume at 4200 ft.

It is well understood that no single attribute can carry enough diagnostic weight to enable discrimination between all of the features or properties of interest in the reservoir. This premise is endorsed by Figure 3 which depicts the similarity attribute.

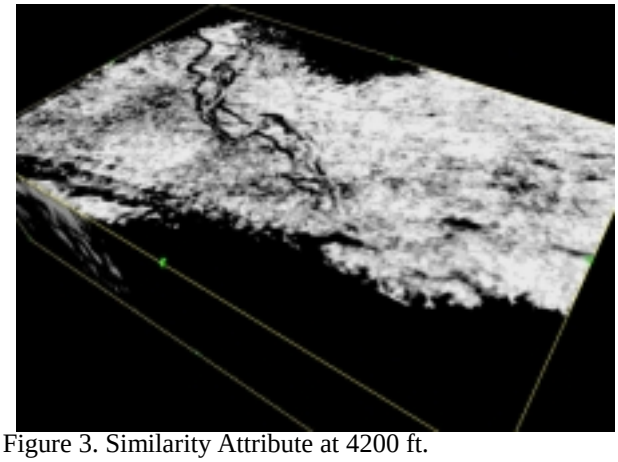

Figure 3. Similarity Attribute at 4200 ft.

Similarity is a coherence class geometric attribute that has been engineered to emphasize the seismic geomorphology and in this example provides useful insights into the morphology of this fluvio-deltaic system.

Although the coherence class attribute enables us to make a more informed interpretation of the geometry of channeling through the Vicksburg reservoir, it tells us nothing about the physical properties in the reservoir, i.e.

what's in the channel? Is it sand or shale, what are the fluids, saturation, porosity, etc.?

To address the problem of distinguishing between sands and shales in the absence of well calibration tools, or when the impedance contrasts of the two dominant lithologies is similar, an *a priori* hybrid attribute has been developed that explicitly defines a shale based on its depositional characteristics. For example, a shale, in a clastic environment often exhibits lateral continuity, a high degree of parallel bedding and occur as thin laminae which, in general, cause a higher seismic spectral signature than surrounding lithologies.

The definition of a shale as having specific seismic characteristics allows for the derivation of a rule-based hybrid attribute. Therefore, a fuzzy scale of 0 to 1 can be established for values based on compliance with the declared depositional and spectral characteristics. Thus, value of 1 would represent strict compliance, and therefore be indicative of a highly shale-prone lithology whereas a value of zero would represent highly non-shale-prone lithologies. In this latter case, one might reasonably infer the presence of a sand or a carbonate. The hybrid attribute is assembled from of a suite of "physical" and "geometric" attributes that, on a sample by sample basis, analyze the seismic data for lateral continuity, parallelism (via dip-scanning) and bandwidth.

The shale indicator hybrid attribute volume is exhibited in Figure 4. In this example, the darker end of the grayscale color spectrum is more shale prone and the lighter color is more non-shale prone. Note, the possible shale-filled channel and the correlation between the lighter colors and the likely locations of point bars.

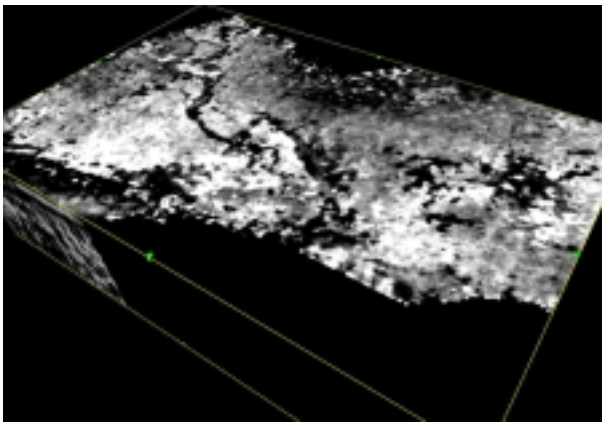

Figure 4. Shale Indicator attribute at 4200 ft.

The shale indicator allows us to differentiate between shales and non-shales in a clastic setting, Another independently computed seismic attribute that can also assist in this task is the relative acoustic impedance attribute. In the absence of low frequency information derived from a local well, this attribute is useful for providing insights into the variability of band-limited acoustic impedance.

In the Vicksburg example, the shales exhibit a higher acoustic impedance that the sands. The relative acoustic impedance attribute volume exhibited in Figure 5 shows a high degree of correlation between the shale-prone predictions made from the Shale Indicator attribute and the higher impedance (blue) areas in the relative acoustic impedance attribute. The lower impedances are colored yellow and it is interesting to note that these pick out possible "sweet spots" in the point bars as well as a possible deltaic facies in the south-east part of the asset.

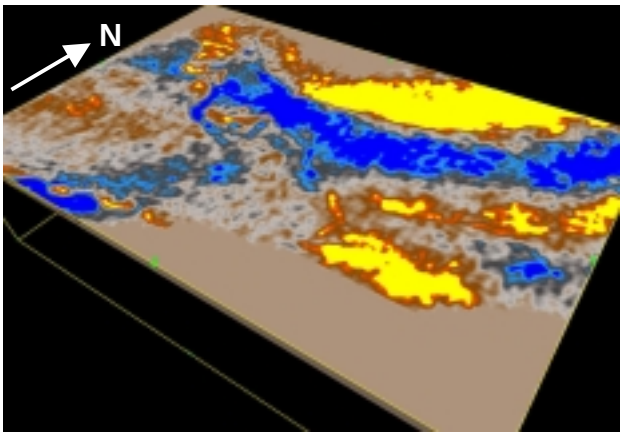

Figure 5. Relative Acoustic Impedance attribute at 4200 ft. (low impedance is yellow, high impedance is blue).

Having identified a number of qualitatively interesting features, a suite of 8 attributes was then input to the K-SOM classifier to examine each seismic sample in a statistical sense for similarities in net multi-attribute response. Figure 6 shows the results of a classification using a 10 x 10 (100 class) Kohonen network topology.

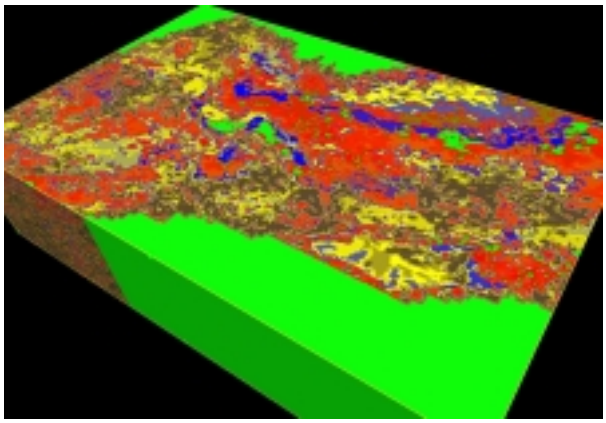

Figure 6. Kohonen (10 x 10) classification at 4200 ft.

Note that we see a general increase in "order" within the data, and the appearance of a number of patterns with distinct geologic form. Unfortunately, as is common with this type of algorithm, it is not possible to directly infer reservoir properties from this interpretation.

The same network topology was imposed on multiple log curves acquired at each of the 4 wells. The 100 log-derived Kohonen classes were then distilled down to a more manageable set of 6 classes based upon physically and acoustically relevant properties, such acoustic impedance, Poisson's ratio, volume shale, water saturation,

etc. The classes are shale, silt, 2 low quality sands, wet sand and pay sand. Figure-7 shows the Kohonen Volume after calibration using the 4 wells. The volume illustrates an additional level of order within the grouping. Furthermore, the classification is now directly related to specific classes of lithology, based on our log-based calibration. In this example, "yellow" represents reservoir quality sands, "blue" represents shales and "orange" poor quality silty sands.

This final classified and calibrated volume ties the available well data, and clearly identifies future upside drilling potential. Figure 8 shows the tie between the seismic classes and log-derived reservoir properties at the reservoir zone for one wet and two producing wells.

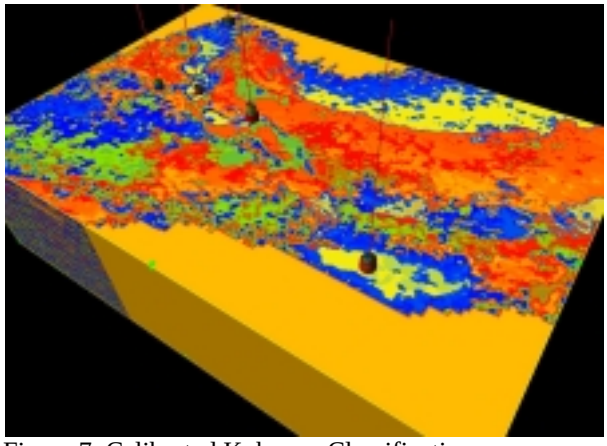

Figure 7. Calibrated Kohonen Classification

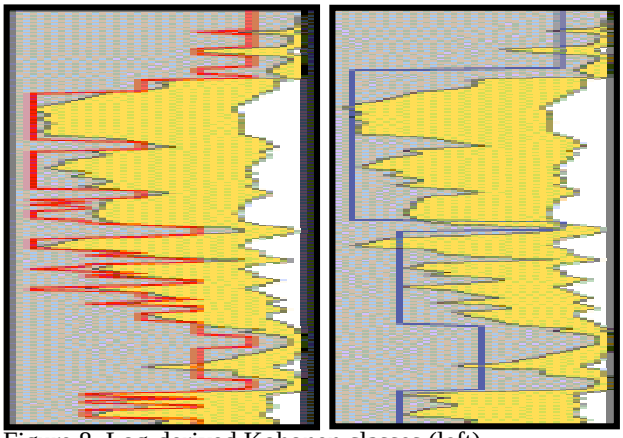

Figure 8. Log-derived Kohonen classes (left) seismic-derived Kohonen classes (right).

Conclusion

This initial study shows much promise for the method for use in seismic reservoir characterization. Quality of the tie between the classified seismic and log-data was high. However, additional drilling would be necessary to confirm these results.

There is considerable scope for further testing and refining of this method, The flexibility of choice as regards input seismic attributes, use of pseudo-wells derived from rock-physics models and topology of the Kohonen network provides for many options for additional study.

References

Morice, M., Keskes, N., Jeanjean, F., 1996, Manual and automatic seismic facies analysis on SISMAGE Tm workstation: Annual Meeting Abstracts, Society Of Exploration Geophysicists, 320-323

Russell, B., Hampson, D., Schuelke, J., Quirein, J., 1997, Multiattribute seismic analysis: The Leading Edge, October, 1439-1443

Taner, M., 1997, Kohonen's self organizing networks with "conscience": Internal paper, Rock Solid Images, www.rocksolidimages.com

Walls, J., Derzhi, N., Dumas, D., Guidish, T., Taner, M. and Taylor, G., 1999, North Sea reservoir characterization using rock physics, seismic attributes, and neural networks: A case history: Annual Meeting Abstracts, Society Of Exploration Geophysicists, 1572-1575

The Rock Physics of Seismic Fluid Attributes

Vaughn L. Ball, Phillips Petroleum
Kevin Northey, Phillips Petroleum
Doug Foster, Phillips Petroleum

Abstract

The tendency for a rock to change its bulk properties upon fluid substitution is its "Fluid Sensitivity", and is an intrinsic property of the rock. The magnitude of the change in bulk rock properties is predictably related to changes in seismic reflection attributes. These changes are often called the "fluid effect". We can speak of a fluid effect in relation to the classic "A", "B", and "C" coefficients of the Aki & Richards linearization. Fluid sensitivity and fluid effect are often qualitatively related to porosity and P-wave velocity, but can be more precisely related to an important property of porous rocks called the "Biot Coefficient". For most seismic attributes, the fluid effect is independent of the surrounding lithology. Only the fluid effect for the "B" attribute has a component that depends on surrounding rocks. The fluid effect for seismic attributes are separable in relation to properties of the rock, and properties of the fluid, and can be expressed as the product of rock properties and fluid properties.

Introduction

Seismic detectability of pore fluids is a function of two factors: 1) The magnitude of the change in seismic attributes upon fluid substitution, and 2) The value of the fluid seismic attribute compared with the background attribute population.

The value of a fluid seismic attribute is a consequence of the initial wet response, and the magnitude of the change caused by fluid substitution. The starting position represents the lithologic component of the response, while the magnitude of the change represents the fluid component of the response. Where the fluid effect is small, the lithologic component dominates, and the ability to detect hydrocarbons is small regardless of the position of the final response within the reflectivity population.

Fluid detectability, as contrasted with **lithology discrimination**, requires that the change in seismic attributes between the wet and hydrocarbon cases be large relative to the reference attribute population. This change in reflection magnitude is the "fluid effect". Using a map-view perspective rather than a section perspective can increase detectability by reducing the width of the reference attribute population, but the same fundamental principle applies: greater fluid effect equates to greater fluid detectability.

It is the objective of this paper to expose the rock properties that control the magnitude of the fluid effect for each of the three Aki & Richards seismic attributes.

Fluid Sensitivity

Replacement of pore waters with hydrocarbon fluids in a reservoir rock results in a change in the bulk modulus and density of the rock. The change in bulk density is readily given by $\rho_b = \phi\ \rho_f$, and for bulk modulus, we might postulate a similar expression

$$K_b = S_f \quad K_f . \tag{1}$$

Here, K_b is the rock bulk modulus, K_f is the fluid bulk modulus, and S_f is the **fluid sensitivity**, yet to be defined. The symbol is used throughout this paper to denote change in properties due to fluid substitution. The classic low frequency theory of Gassmann (1951) and Biot (1956) can be used to obtain an expression for S_f. In Figure 1, the Gassmann equation (2), is used to plot rock bulk modulus as a function of fluid bulk modulus. The near-linearity of this relationship contrasts with the popular perception of the Gassmann equation as highly non-linear. This common misconception is due to the fact that the x-axis is traditionally plotted in terms of fluid saturation, and therefore incorporates highly nonlinear fluid mixing laws into the plot.

It is instructive to write the Gassmann equation for bulk modulus in terms of the Biot coefficient rather than the more usual parameterization in terms of dry frame bulk modulus. This form is given by Mavko et al. (1998).

$$K_b = K_0(1 \quad \beta) + \frac{\beta^2 K_0}{(\beta \quad \phi) K_f + \phi K_0} K_f \tag{2}$$

Here, β is the Biot Coefficient, defined as the ratio of change in pore volume to the change in bulk rock volume under an increment of applied external stress. Other terms in this expression are the rock bulk

modulus, K_b; the porosity, ϕ; the fluid bulk modulus, K_f; and the grain bulk modulus, K_0.

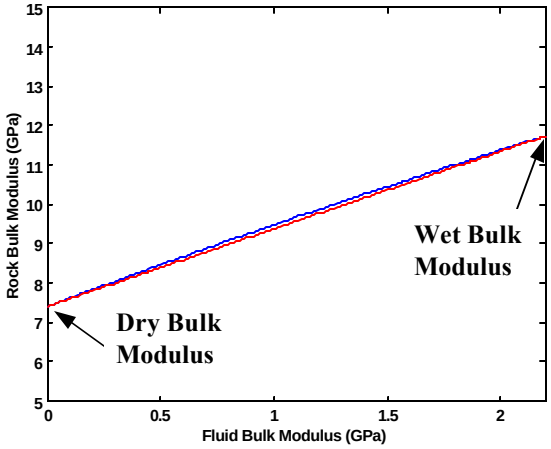

Figure 1. The Gassmann equation predicts a near-linear change in bulk modulus as a function of fluid modulus (top curve). A linear version of the Gassmann equation results in negligible errors.

The Biot Coefficient can be thought of as the "pore softness". A value of 1 indicates that all volumetric contraction occurs in the pore space, and corresponds to the Reuss bound. A value equal to the porosity indicates that the pore space contraction is the same as the grain material, and corresponds to the Voigt Bound. It should be emphasized that equation (2) is entirely equivalent to more traditional forms of the Gassmann equation. This equation can now be readily linearized as follows.

$$K_b = K_0(1 \quad \beta) + \frac{\beta^2 K_0}{(\beta \quad \phi) K_w + \phi K_0} K_f \tag{3}$$

where K_w is the bulk modulus of brine. Equation (3) is linear in terms of the fluid bulk modulus. We define the slope of this line to be the fluid sensitivity and write

$$S_f = \frac{\beta^2 K_0}{(\beta \quad \phi) K_w + \phi K_0} \quad \frac{\beta^2}{\phi} \tag{4}$$

where the approximation is the first term of the Taylor's series expansion, and provides a useful estimate of fluid sensitivity in most situations.

We can now express the change in P-wave modulus due to fluid substitution as the product of the fluid sensitivity and the change in fluid bulk modulus.

$$M = K_b = S_f \; K_f \tag{5}$$

Here $M = \rho V_P^2 = K_b + 4\mu/3$ is the P-wave modulus, and μ is the shear modulus, which is constant for fluid substitution. Equation (5) is critical in the problem of defining the fluid effects of key seismic attributes.

Fluid Effect of Seismic Attributes

Clearly, a change in P-wave modulus due to fluid substitution will affect the seismic response of a reservoir. An understanding of this fluid effect is critical in the problems of fluid detection and fluid discrimination. The most common and important seismic attributes are the coefficients of the Aki & Richards (1980) approximation of the Zoeppritz equations.

$$R_{pp} \quad A + B\sin^2\theta + C \quad \tan^2\theta \quad \sin^2\theta \tag{6}$$

where R_{PP} is the P-wave coefficient expressed as a function of angle of incidence, θ, and the coefficients are defined by

$$A = \frac{1}{4}\ln \; \frac{M_2 \rho_2}{M_1 \rho_1} \div \tag{7}$$

$$B = \frac{1}{4}\ln \; \frac{M_2 \rho_1}{M_1 \rho_2} \div \; 2\frac{V_S^2}{V_P^2}\ln \; \frac{\mu_2}{\mu_1} \div \tag{8}$$

$$C = \frac{1}{4}\ln \; \frac{M_2 \rho_1}{M_1 \rho_2} \div \tag{9}$$

where M is the P-wave modulus, μ is the S-wave modulus, ρ is density, and subscripts are used to indicate the overlying layer (1), and the underlying layer (2). In contrast to the more conventional velocity form, these expressions have been written in terms of elastic moduli, where fluid substitution may be more readily applied.

For the three Aki & Richards seismic attributes, we define the fluid effect to be the change in the attribute upon fluid substitution, (i.e. $A = A' \; A$, where A' is the attribute after fluid substitution) and write

$$A = \frac{1}{4}\left(\frac{M}{\bar{M}} + \frac{\rho_b}{\bar{\rho}_b}\right) \tag{10}$$

$$B = \frac{1}{4}\left(\alpha\frac{M}{\bar{M}} - \frac{\rho_b}{\bar{\rho}_b}\right) \tag{11}$$

$$C = \frac{1}{4}\left(\frac{M}{\bar{M}} - \frac{\rho_b}{\bar{\rho}_b}\right) \tag{12}$$

where α can be thought of as a lithology amplification factor and is expressed as

$$\alpha = 1 + 4\frac{V_S^2}{V_P^2}\ln\left(\frac{\mu_2}{\mu_1}\right) \tag{13}$$

Here, ρ_b denotes the wet bulk density of the reservoir, and the overbar denotes an average of the property before and after fluid substitution. Equations (10) through (13) follow directly from equations (7) through (9) after recognizing that p-wave modulus, reservoir density, and V_S/V_P change upon fluid substitution, while shear modulus does not. Additionally, the derivation of equation (11) requires the approximation

$$\frac{V_S^2}{V_P^2} \approx \frac{1}{2}\left(\frac{V_S^2}{V_P^2} + \frac{M}{\bar{M}}\right) \tag{14}$$

Three important observations can be made regarding equations (10) through (13).

1. The fluid effect for the A and C attributes is independent of the properties of the surrounding lithologies, and depends only on the properties of the reservoir before and after substitution.

2. The fluid effect for the B attribute involves a lithology-related term that acts as an amplifier for the modulus fluid effect. In particular, an increase in shear modulus into the reservoir will result in an amplification of the fluid effect, while a decrease in shear modulus will result in a diminished fluid response.

3. The density effect constructively adds to the modulus effect for the A attribute, while it destructively adds for the B and C attributes.

Separation of fluid and rock properties

We can separate reservoir rock properties from fluid properties in equations (10) through (12) as follows:

$$A = \frac{1}{4}\left(R_M\left(K_f + R_r\right) + \rho_f\right) \tag{15}$$

$$B = \frac{1}{4}\left(\alpha R_M\left(K_f - R_r\right) - \rho_f\right) \tag{16}$$

$$C = \frac{1}{4}\left(R_M\left(K_f - R_r\right) - \rho_f\right) \tag{17}$$

where R_M and R_r are reservoir rock properties that act as multipliers for changes in fluid modulus and fluid density. These can be called the "modulus reactance", and the "density reactance", and are given by

$$R_M \approx \frac{S_f}{M\left(S_f/2\right)} \tag{18}$$

$$R_r \approx \frac{\phi}{\rho_b\left(\phi/4\right)} \tag{19}$$

Definition (18) follows from equation (5), while definition (19) follows from $\rho_b = \phi\,\rho_f$. The denominators in these equations are a reasonable approximation to average reservoir properties before and after fluid substitution.

Fluid Effect in the A-B Plane

The Fluid Effect in the A-B Plane can now be separated into three component vectors, one due to change in density, one due to change in fluid modulus, and the last due to lithology contrast across the interface. These effects are shown graphically in Figure 2. The density response is always up to the left, and is independent of surrounding rock properties. The modulus response is always down to the left if there is no contrast in shear modulus across the interface. Finally, the lithology effect is a vertical vector whose sense is controlled by the change in shear modulus across the interface, and whose magnitude is controlled by the V_S/V_P ratio as expressed in equation (13).

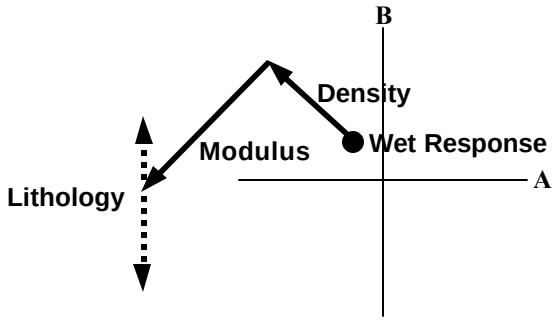

Figure 2. The Fluid Effect in the A-B plane is decomposed into a density effect (exaggerated), modulus effect, and lithology amplification of the B term.

Figure 3 compares the fluid response of a sand set within comparably "hard" shale with the response of the **same** sand set within comparatively "soft" shale. The fluid effects are the same in both cases, but the positive increase in shear modulus for case two results in an amplification of the fluid effect for the B term.

Conclusions

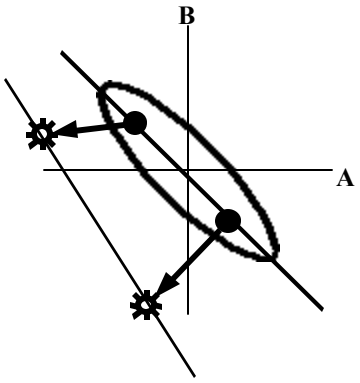

Figure 3. A sand situated within low impedance shales will have a strong B-term Fluid effect than it would if situated within high impedance shales.

The magnitude of change in reflection coefficient with fluid substitution is directly related to the ability to seismically detect fluids in the subsurface. The magnitude of this change depends on intrinsic properties of the rock, coupled with the difference between density and bulk modulus of the substituting fluid and water properties. The rock properties that determine this response are derived properties, and depend primarily on the density and fluid sensitivity of the reservoir. The fluid effect for the B attribute is influenced by the contrast in shear modulus across the reflecting interface, where an increase in shear modulus results in an amplification of the fluid effect.

References

Biot, M. A., 1956, Theory of propagation of elastic waves in a fluid saturated porous solid: J. Acoust. Soc. Amer., **28**, 168-178.

Gassmann, F., 1951, Uber die elastizitat poroser medien: Vier. der Natur Gesellshaft, **96**, 1-23.

Mavko, G., Mukerji, T., and Dvorkin, J., 1998, The Rock Physics Handbook: Cambridge University Press.

Aki, K., and Richards, P. G., 1980, Quantitative Seismology: Theory and Methods, W. H. Freeman and Co., 932 pp.

Acknowledgements

The authors would like to thank Phillips Petroleum Company for permission to publish this paper. We are also grateful for input and discussions with Herb Swan and Brackin Smith.